In Situ Investigation of Failure in 3D Braided SiC_f/SiC Composites under Flexural Loading

Changqi Liu [1], Yang Chen [2], Duoqi Shi [1, *], James Marrow [2, *], Xin Jing [3], Xiaoguang Yang [1]

[1] School of Energy and Power Engineering, Beihang University, Beijing 100191, China

[2] Department of Materials, University of Oxford, Oxford, OX1 3PH, UK

[3] School of Power and Energy, Northwestern Polytechnical University, Xi'an, 710072, China

Abstract

The mechanical failure of three-dimensional (3D) 4-step braided SiC_f/SiC composites, processed by precursor infiltration pyrolysis, has been studied under flexural loading to investigate the condition at failure. The investigation integrated the advantages of continuous data acquisition by optical imaging and 3D reconstruction of internal structure in X-CT imaging, for in situ investigation of microstructure-related failure mechanisms. Optical imaging with digital image correlation acquired the surface displacements. X-ray computed tomographs, obtained in situ, were analysed by digital volume correlation to measure the 3D displacement fields. Image subtraction, informed by the 3D displacements, was used to detect and visualize crack development. Curvature measurement, via the displacement fields, monitored the change in effective flexural modulus. The observed failure modes included matrix cracking, inter- and intra-bundle debonding and fibre breakage. Tensile cracks were arrested by the

* Corresponding authors

E-mail address: shdq@buaa.edu.cn; james.marrow@ox.ac.uk

heterogeneous microstructure, and the ultimate failure under flexural loading was due to multiple cracking in compression.

Keywords

SiC/SiC, Braided composites, X-ray computed tomography, Digital image correlation, Flexural loading, Failure

1. Introduction

For more than twenty years, ceramic matrix composites (CMCs) have been considered as a potential replacement for metallic alloys in aerospace applications [1,2]. Especially for high-temperature components in the aircraft engines, it is vital for materials to retain good mechanical properties under extreme temperatures and chemically corrosive environments [3]. SiC_f/SiC composites have attracted much attention due to their non-brittle behaviour, high specific strength, creep resistance and oxidation resistance [4]. The use of SiC_f/SiC composites for aircraft engines has progressed from the exhaust components to shrouds/seals, combustors, stators/vanes, and finally to the most demanding application of rotors and blades [5]. To take maximum advantage of the performance of SiC_f/SiC composites in engineering structures, continuous fibre bundles (scale 0.1–1 mm) are usually braided in custom-designed 3D patterns. 3D 4-step braided patterns have been developed due to their light weight and excellent structural integrity and mechanical properties [6–8]. The fibre bundles are oriented to follow the primary load paths expected in the designed component to maximize its stiffness and

strength, and are interlocked to prevent catastrophic separation when damaged. The mechanical behaviours of SiC_f/SiC composites have been studied both at room and elevated temperatures, and general reviews of their properties, including monotonic tension, fatigue and creep behaviour are given in [5,9].

SiC fibres are usually coated by chemical vapor deposition (CVD) with BN or PyC and may have a protective layer of either SiC or Si_3N_4 [10]. The SiC matrix can be obtained by one or more of the following: chemical vapor infiltration (CVI) [11], reactive melt infiltration (RMI) [12], polymer impregnation and pyrolysis (PIP) [13], slurry infiltration (SI) and the nano-infiltration and transient eutectic phase (NITE) method [14]. Two primary SiC_f/SiC fabrication routes are currently used to produce complex-shaped components for aerospace engines, with microstructures capable of reliable structural operation for long times at elevated temperatures, one was developed under the NASA Enabling Propulsion Materials (EPM) Program [15] and the other was developed and demonstrated by General Electric [12]. Both routes use the CVI and RMI methods. However, the excess silicon that remains in the matrix produced in the final silicon infiltration step intrinsically limits the CMCs upper-use temperature to 1250°C [16]. To solve this problem, a PIP or CVI-PIP approach has been adopted recently. The PIP method has the advantages of lower pyrolysis temperature, low cost, and a homogeneous ceramic matrix, and it is suitable for large-scale component fabrication [17]. However, SiC_f/SiC composites fabricated by PIP usually have a relatively high total porosity (10-15%), and it is important to understand how this porosity affects the mechanical properties. Recently, 3D SiC_f/SiC composites prepared via PIP have been

studied to investigate the effect of heat treatment and interface phases on their mechanical properties at ambient [18,19] and high temperatures, including creep [20,21]. These studies have shown that a suitable heat treatment temperature (1400°C) and interface thickness (0.1 μm) can improve mechanical properties such as flexural strength and fracture toughness significantly. Composites prepared by PIP using such optimized parameters also exhibited excellent tensile and creep behaviours at room and elevated temperatures. Local effects such as the fibre directionality have also been investigated in [22], as has the influence of film cooling holes at 1350°C in air [23]. These studies indicated these local effects have a stronger influence on dynamic and long-term properties than static and short-term properties.

Macroscopic tests are useful to assess the average properties of composites and are an important data source for engineering applications. For deeper understanding it is vital to observe how the damage initiates and propagates during mechanical tests. Digital image correlation (DIC) is a non-contact optical technique to acquire in situ information of the surface displacement and strain fields. It has been widely used in mechanical testing of ceramic composites. For instance, DIC has been used to identify the locations of cracks and measure crack opening displacement profiles in SiC_f/SiC composites during tension tests [24]. Observations of the local deformations were used to study the influence of weave architecture in tensile loading of SiO_{2f}/SiO_2 composites [25]. It has been applied to capture the evolution of displacement and strain fields of 3D needle-punched C/SiC composites during three-point bending tests [26], and to investigate the non-uniform strains of a 2.5D woven SiO_{2f}/SiO_2 composites in tension [27]. The tensile

behaviours of notched SiC_f/SiC and Al_2O_{3f} /Al_2O_3-SiO_2 composites have been examined [28,29] and damage mechanisms of a 2D braided SiC_f/SiC tube were studied at the tow scale under tensile loading [30].

For CMCs with complex 3D braided structures, surface investigation methods are insufficient to investigate failure mechanisms that are related to the internal microstructures. X-ray computed tomography (X-CT) can provide volumetric information on the microstructure of complex materials and has been applied in qualitative examinations of the porosity and microstructures of a range of CMCs [17,31–33]. In situ studies allow damage evolution to be observed, and can support the use of image-based simulations to understand the effects of microstructure on crack initiation [34,35]. In situ X-CT has been used to characterize damage development within CMCs including C_f/C-SiC, SiC_f/SiC and C_f/SiC under compressive [36], tensile [3,37], flexural [38] and fatigue loading [39]. Digital volume correlation (DVC) analysis, applied to in situ X-CT data, uses the inherent features of the microstructure to measure the 3D displacements and strains [40]. Post-processing of the data can also allow discontinuities such as cracks to be detected from the local residual differences between the reference and deformed volumes [41], and then to extract networks of cracks within complex initial architectures [42]. Coupled in situ X-CT and DVC analysis has been utilized to investigate the microstructure-dependent damage mechanisms in braided SiC_f/SiC composite tubes under tensile and compressive loading [43,44], and some studies that have also applied DVC and X-CT to flexural

loading, such as carbon/epoxy [45] and C/C-SiC composites [46]. No such studies have been conducted on 3D braided SiC/SiC composites under flexural loading.

In this paper, 3-point bend flexure tests of two similar types of 3D 4-step braided SiC_f/SiC composites, produced by precursor infiltration pyrolysis, have been observed in situ using optical and X-CT imaging, and analysed by image correlation. The objective of this study is to investigate the 3D deformation characteristics and the initiation and propagation of damage within the microstructure of SiC/PyC/SiC composites under flexural loading. This knowledge can provide guidance for the optimization of processes in material preparation. Additionally, the study contributes to the development of image-based methods to quantify damage on the macroscopic scale that may facilitate real-time monitoring of these materials in engineering applications.

2. Materials and experiments

2.1 Materials and Specimens

Two batches of specimens were studied; both were 3D 4-step braided SiC_f/SiC composites fabricated by the precursor infiltration pyrolysis (PIP) process. The first batch of composite specimens (Series 1, a total of 4 specimens), with an approximate size of 80 mm×10 mm×3.75 mm was tested at room temperature, with observation by single-camera DIC. The other batch of composite specimens (Series 2, a total of 4 specimens) had approximate dimensions of 45 mm×5 mm×3.5 mm and was tested at room temperature with observation by in situ X-CT for DVC analysis.

The two batches were fabricated by similar methods (Table 1). The Series 1 and Series 2 specimens utilized KD-I and KD-II SiC fibres respectively, with the KD-II fibres being of higher strength and stiffness. The KD-I fibres have high oxygen content (12 wt% – 13 wt%), and exhibit greater variation of mechanical properties and lower thermal stability [47]. The KD-II fibres have significantly reduced oxygen content (only about 1 wt%), and can maintain high tensile strength and modulus below 1500℃ under an inert atmosphere [48]. In both batches, a pyrolytic carbon (PyC) layer was first deposited on the fibre preform using Propylene (C_3H_6) at 850°C and 2 kPa for 10 h. The SiC matrix was prepared by the PIP route, with the coated fibre preform infiltrated by LPVCS or 50 wt% PCS/xylene solution under vacuum for 2 h. After drying, the preform was pyrolysised above 1000℃ for 1 h under a protective Ar atmosphere. The PIP process was repeated until the weight increase of the composite in a cycle was less than 1%.

2.2 Flexural loading with DIC (Series 1 Composite)

3-point bend flexure tests with span to thickness ratio of ~20 and ~16 were conducted on specimens of the Series 1 composite in an electronic universal testing machine (WDW-100) with a force measurement range of ±100 kN, at a cross-head speed of 0.5 mm/min [49][50]. Single-camera DIC was used in the tests with the span to thickness ratio of 20, in which one side of the specimen was sprayed with white and black paint to produce uniform, random speckles and a CCD camera (1280×1024 pixels) with a lens (focal length 35 mm) recorded images at a frame rate of 7 fps, with a 10 μm pixel

size (i.e. field of view ~13×10 mm). The experimental setup for the flexural tests with DIC is shown in Fig. 1a. DIC analysis of a region of interest (ROI), measuring 12.2 mm×3.3 mm used the software VIC-2D (Correlated Solutions), with an image subset (correlation domain) dimension of 29×29 pixels and step size (correlation point spacing) of 5 pixels. The image at a preload of 20 N was the reference, and rigid body movements were removed relative to a reference point chosen within the ROI.

2.3 Flexural loading with in situ X-CT and DVC (Series 2 Composite)

3-point bend flexure tests of the Series 2 composite with 20 mm span (i.e. span to thickness ratio of ~6) were performed using a Deben CT5000 loading rig (5 kN load capacity, glassy carbon loading pins) that was designed for in situ X-CT. The experimental system for flexural tests with in situ X-CT is shown in Fig. 1b. Two specimens were first tested with continuous monotonic loading (0.2 mm/min) to obtain the load-displacement behaviour, based on which the loads for subsequent in situ observations were selected. The loading rig was mounted on the rotational stage of an Xradia 510 Versa X-ray microscope. Two specimens were each observed by X-CT at a pre-load of 30 N and then at progressively higher loads. This was increased between observations using a cross-head speed of 0.2 mm/min, and tomographs were recorded at fixed cross-head displacements. The microscope was operated at an X-ray energy of 80 keV and power of 7 W, with 0.4× objective to obtain an image voxel size of 7.2 μm with 1× binning of the 2048 × 2048 camera. Each scan of 1601 projections, recorded over a 360° rotation with 40 s exposure per projection, required 19 h 15 min. The

tomography reconstruction used the Zeiss software. Before image processing in Avizo Fire software and DVC analysis with LaVision Davis software, the reconstructed images were cropped to 1700×630×850 voxels (i.e. 12.2×4.5×6.1 mm) and resampled from 32 bit to 8 bit using FiJi/ImageJ[1].

The DVC analysis used the tomograph at 30 N pre-load as the reference. The DVC analyses were conducted using the same parameters for each loading step, with an initial subset size (correlation domain) of 192×192×192 voxels (75% overlap, 1 pass, i.e. correlation step size 48 voxels), then 96×96×96 voxels (75% overlap, 2 passes), and finally 48×48×48 voxels (75% overlap, 2 passes, i.e. correlation step size 12 voxels). Rigid body movements, relative to a fixed reference point, were removed.

Pores in the X-CT images have similar contrast with cracks, and as pores and cracks are usually connected, it is difficult to extract and visualize the cracks by threshold-based image segmentation methods. Furthermore, cracks with narrow opening have low contrast and can be difficult to observe clearly in X-CT images. Image subtraction has been applied to address this, by a novel approach that is informed by the DVC measurements. A detailed introduction to this method can be found in reference [42]. Briefly, the deformed images are transformed into the configuration of the reference image, according to the local transformation field measured by DVC, and image subtraction is conducted within the reference configuration. Newly created features,

[1] Schindelin, J.; Arganda-Carreras, I. & Frise, E. et al. (2012), "Fiji: an open-source platform for biological-image analysis", Nature methods 9(7): 676-682, PMID 22743772, doi:10.1038/nmeth.2019

such as cracks, can then be highlighted within the subtraction results (referred to as subtracted images), as the contrast from the initial microstructural features, such as pores and pre-existing cracks, is removed. This method was used to visualize the development of damage. In the present work, the displacement field measured by DaVis software was imported into an in-house code CMV3D to perform image subtraction [Chateau,Strain,2018].

3. Results

3.1 Series 1 Composite (Flexural loading with DIC)

The nominal tensile stress, σ, and strain, ε, were calculated using standard Euler beam theory [49] from the load-displacement data and the nominal stress-strain curves of four Series 1 specimens (1-1 – 1-4) are shown in Fig. 2a. The experimental conditions and measured mechanical properties of the Series 1 specimens are summarised in Table 2. Specimens 1-1 and 1-2 were tested with span to thickness ratio of 20 (the results are presented in the form of solid lines), and specimens 1-3 and 1-4 were tested with span to thickness ratio of 16 (the results are presented as dash dot lines). The apparent elastic modulus obtained in the linear region (tangent modulus) varies between specimens and is of the order of 80 to 90 GPa. Fig. 2b shows optical images of the four Series 1 specimens (1-1 – 1-4) captured at their peak loads. More severe debonding can be observed in the shorter span specimens 1-3 and 1-4 compared with the longer span specimens 1-1 and 1-2. The measured flexural strength is slightly greater in the specimens with the higher span to thickness ratio.

As the general flexural behaviour and damage evolution is similar in all specimens only a detailed analysis of specimen 1-1 will be presented. The nominal tensile stress-strain curve of specimen 1-1 is reproduced in Fig 3a, where points are identified that correspond to: a) the start of the nonlinear stage; b) the occurrence of interlayer debonding; c) the peak load; and d) the post-failure condition. This specimen shows linear behaviour below 450 MPa, then some nonlinearity before the maximum stress (flexural strength, 650 MPa) is reached. Optical images recorded during the testing of specimen 1-1 (Fig. 3b – e) show that as the load increased, damage was first observed to occur near to the tensile surface, opposite the loading pin (Fig. 3b, σ=446 MPa, point a of Fig. 3a). The second failure mode was interlayer debonding near the loading pin on the compressive surface (Fig. 3c, σ=613 MPa, point b of Fig. 3a). The debonding developed further at the compressive surface, causing surface extrusion and buckling (Fig. 3d, σ=648 MPa, point c of Fig. 3a). The debonding then extended towards the tensile side (Fig. 3e, after failure, point d of Fig. 3a) until the specimen lost the ability to carry a higher load, which lead to a dramatic drop of the load in the macroscopic curve.

Displacements fields were measured in the *XY* plane by DIC, and maps of the component parallel to the loading direction (*Y* direction), are shown in Fig. 4. They generally exhibit the typical patterns of three-point bending, with the bending centred at the position of the loading pin (*X*=5.1 mm), which is marked by black dotted lines. For a beam in flexure with a high span-to-thickness ratio, the normal stress perpendicular to the cross section (ε_{XX}) is dominant. The strain fields were calculated

from the full field displacements using a centred 3-point differentiation scheme, and Fig. 5 maps the evolution of the ε_{XX} component with increasing flexural stress within the ROI. The strain distribution was initially almost uniform (Fig. 5a), with tensile and compressive strains roughly symmetric (i.e. across the expected location of the elastic neutral axis). As the flexural stress increased, the tensile and compressive strains increased in magnitude (Fig. 5b and c). As the tensile stress reached 450 MPa, significant local strain concentrations developed at the tensile surface (Fig. 5d), and became extremely inhomogeneous as the tensile stress reached 643 MPa (Fig. 5f).

Fig. 5g shows the position of the neutral axis with increasing applied flexural stress. In flexure, to maintain static equilibrium, the neutral axis is closer to the surface with higher elastic modulus. It is initially 0.12 ± 0.07 mm below the centre line of the specimen, which is consistent with the tensile elastic modulus of braided composites being higher than the compressive elastic modulus [51]. The neutral axis moved across the centre line as the flexural stress increased, indicating increased compliance at the lower tensile surface due to damage, and it was located 0.24 ± 0.06 mm above the centre line when the stress reached 300 MPa. Obvious damage occurred on the compressive side (Fig. 3c) when the stress was 643 MPa, and the neutral axis returned towards the centre line due to the increased compliance of the damaged compressive region.

According to Euler theory for a slender, homogeneous and linear elastic beam, the elastic modulus can be obtained from the radius of curvature, ρ, which is related to the bending moment, M, elastic modulus, E and second moment of area, I, (Eq. 1) via the

linear gradient of tensile strain across the beam. This provides a method to estimate the effective elastic modulus, directly from the DIC observations; the small movement of the neutral axis relative to the centre line, due to inhomogeneous elastic properties, is neglected. To reduce the effect of DIC errors, the average strain at the mid-span was obtained from the relative displacement change, ΔX, between two *YZ* planes symmetrically located on either side of upper loading pin and separated by a gauge length, l_c, of 4 mm. Over this distance, the bending moment is within 95% of its maximum.

$$\frac{1}{\rho}=\frac{\varepsilon_{xx}}{Y}=\frac{M}{EI} \tag{1}$$

The strains, normalized by *M/I,* are shown in Fig. 6a, with a linear best fit applied. Its gradient provides the effective elastic modulus, which is presented in Fig. 6b as a function of the applied stress. The DIC-obtained elastic modulus for specimen 1-1 at low stress was 97.9±1.1 GPa. It did not change significantly until 450 MPa, when visible damage appeared on the tensile surface (Fig. 3a). Here the elastic modulus reduced to 86.4±0.7 GPa, and then declined to 56.5±1.7 GPa at 643 MPa with the occurrence of the mass of damage at the compressive surface (Fig. 3c). The same trend is observed in the modulus that was calculated from the local gradient of the nominal stress/strain (labelled as 'Experimental Curve (tangent modulus)'), but this shows a lower initial modulus of 91.9±0.8 GPa. The secant modulus (i.e. gradient from the origin to points on the stress-strain curve) is close to the tangent modulus. Specimen 1-

2 was analysed in the same manner, and showed a similar decline in modulus with applied stress from a lower initial value of 78.2±0.5 GPa.

3.2 Series 2 Composite (Flexural loading with in situ X-CT and DVC)

Load vs displacement data for specimens of the **Series 2** composite are shown in Fig. 7. Due to the shorter span, a progressive quasi-brittle failure was observed after the peak load was attained. The average flexural strength was 709±34 MPa. From the tests on specimens 2-1 (strength 685.2 MPa) and 2-2 (strength 763.3 MPa), loads were selected for the in situ X-CT scans of specimens 2-3 and 2-4, as indicated by circles. The load dropped by a small degree (less than 15%) during each scan. Specimen 2-3 was scanned at 30, 1100, 1250, 1447 N (peak load, strength 677.5 MPa) and at 1033 N after the peak load. These are labelled in sequence (Fig. 7) as scanning steps 0 to 4. Specimen 2-4 was scanned at the loads of 30, 600 and 1100 N and then at 606 N after the peak load of 1597 N (strength 707.6 MPa). The scanning steps are labelled similarly.

A 3D visualization of specimen 2-3, scanned at step 4 (i.e. after the peak load) is shown in Fig. 8a with representative 2D slices in the orthogonal *XY* (Fig. 8b) and *YZ* (Fig. 8c) planes, indicated by red and green traces respectively (the *XZ* slice is approximately 0.35 mm from the compressive surface). The loading pin location on the upper compressive surface is marked by black dotted lines. There are only a few small cracks (indicated by red arrows in the Fig. 8a) at the tensile side, but there is a mass of long cracks, parallel to the directions of fibre bundles, close to the compressive surface. Its development is illustrated in more detail in Fig. 9a, which shows the same vertical *XY*

section at different loads, with zoomed images of local regions (marked by red dotted boxes). There was no visible damage near the compressive surface before 1250 N (step 2). At the peak load (step 3, 1447 N), fibre breakage occurred in the fibre bundles closest to the loading pin. This damage is indicated by yellow arrows in Fig. 9a, which can also be seen in Fig. 8c. Transverse cracks between and within fibre bundles were found in the vicinity of these broken fibre bundles, which are indicated by blue and green arrows respectively in Fig. 9a. These transverse cracks, stemming from interfacial debonding, propagated along the direction of fibre bundles. As the load increased, further intra-bundle cracking developed, and the damaged region increased in size until final failure of the specimen. A series of horizontal *YZ* slices at different loads, at the same location close to tensile surface (about 0.07 mm), are shown in Fig. 9b. Some small surface cracks initiated in the matrix region, on either side of the loading point (indicated by red arrows in the Fig. 9b), when the load reached 1100 N (step 1). The specimen porosity is low in the surface regions [see Supplementary information]. As the load increased, the number of matrix cracks increased, as shown by the increase in the number of red arrows. Moreover, they propagated into fibre bundles, which are indicated by the yellow arrows in Fig. 9b. However, these cracks did not continue to propagate deeper into the specimen and remained close to the tensile surface. A similar pattern of damage was observed in specimen 2-4.

Example displacement fields, relative to the preload (step 0) that were obtained by DVC analysis at 1100 N (step 1) and at the peak load (step 3, 1447 N), are shown in Fig. 10 for specimen 2-3. They confirm the quasi-uniform bending of the specimen before

failure, and also show the effect of damage on the specimen's deformation. The 3D maximum principal strain fields for specimen 2-3 are shown in Fig. 11a at different loads. At 1100 N (step 1) and 1250 N (step 2), the strain distribution generally corresponds to the periodic mesoscopic structure of the composite, and a small number of strain concentrations emerge on the upper and lower surfaces. At peak load (step 3, 1447 N), a major strain concentration develops at the compressive surface, indicating a discontinuity in the displacement field due to damage. In the corresponding subtracted images (Fig. 11b), the formation of a small number of new cracks (labelled in dark red) can be seen from 1100 N at the tensile side. These do not propagate significantly with increasing load. Cracks that were aligned to the direction of fibre bundles have been labeled in green. They developed from 1100 N on the compressive surface, close to the contact of the upper loading pin, and then extended to one side of the pin into a mass of damage with increasing load. The image subtraction result for specimen 2-4 after failure (step 3) is also shown in Fig. 11c, and it exhibits a similar pattern of damage.

The axial strains (ε_{XX}) in the vicinity of the loading pin were calculated using the net *X*-displacements between the two *Y-Z* planes that were located on either side with a distance of 4 mm (centred at *X*=6.1 mm). Over this distance, the bending moment is within 20% of its maximum value; the distance was chosen to reduce uncertainties from the heterogeneity of the displacement field. The strain (normalized by *M/I*, where *M* is obtained for the maximum load at the start of the X-CT scan), is mapped in Fig. 12 at different applied loads for specimen 2-3. It is quite constant in the Z-direction, confirming the uniform bending. The neutral axis is above the centre line at step1 and

step2 (Fig. 12a and b), indicating increased compliance at the lower tensile surface due to damage. Obvious damage occurred at the compressive side at step 3 and developed gradually at step 4, which resulted in movement of the neutral axis towards the tensile side (as shown in Fig. 12c and d). The variation, with *Y,* of the normalized strains, averaged in the *Z*-direction, is shown for specimen 2-3 in Fig. 13a, and the effective elastic modulus was estimated from the gradient as before. The modulus was almost constant prior to the peak load (131.4±1.7 GPa at step 1 and 125.4±1.2 GPa at step 2), and then decreased significantly with increasing applied cross-head displacement. The volume fraction of cracks, obtained by dividing the number of crack voxels identified in the image subtraction results of Fig. 11b, by the number of voxels in the ROI, increased simultaneously with the decrease in modulus (Fig. 13b). Similar behaviour was observed also for specimen 2-4, which had a modulus of 133.5±6.3 GPa (step 1) and 131.9±8.6 GPa (step 2) before significant damage was detected.

3.3 Discussion

The effective elastic modulus obtained for the Series 1 composite using DIC measurement of the specimen curvature agrees well with that derived from the load-displacement data (Fig. 6b), using either local gradient or secant (the latter is more analogous to the DIC measurement); flexural specimens with long span have high compliance so the displacement contribution from the loading rig is small, and a span-to-thickness ratio greater than 16 is recommended [49] for property measurement. The short span used in the testing of the Series 2 composites, which is imposed by the

requirements of in situ X-CT, is shorter than the standard recommendation for reliable modulus measurements [49][50]. The effective moduli for both Series 1 and Series 2 composites, obtained by DIC and DVC analysis of displacement fields, assume isotopic and uniform properties and may therefore only provide approximate values. Nonetheless, the analysis allow the effect of mechanical damage on the specimen compliance to be monitored through its effect on curvature. This method has been applied successfully in flexural tests of polymer composites [52], C/C-SiC composites [46], and alumina-alumina composites [53]. Moreover, this approach, which provided data also on the position of the neutral axis, has potential use as a means to verify numerical simulations of damage development.

The higher effective modulus of the Series 2 composite compared to the Series 1 material, obtained prior to the development of visible damage, is consistent with the higher stiffness of the KD-II SiC fibres [47][48]. This is also consistent with the observation in [54] that SiC fibres significantly affect the flexural properties of SiC/SiC composites. However, differences may also arise from development of the matrix via PIP with alternative precursors (**Table 1**). The distinction of bending strength between specimens 1-1, 1-2 and 1-3, 1-4 may be due to different span to thickness ratios. A relatively small span thickness ratio can encourage shear failure [49], which can be also indicated by the more extensive debonding damage observed in specimens 1-3 and 1-4 in Fig. 2b. The effective flexural modulus difference between Series 1 is quite significant. This may be due to a larger property variations of KD-I fibres [54], but also may arise from heterogeneity of the braided composite microstructure (such as the pores)

and the small thickness of the test specimens, which limits the strained volume. Significant variations in elastic modulus have also been reported in tensile testing of similar materials [51].

In both the Series 1 and Series 2 composite materials, damage first initiated on the tensile side, but the final failure coincided with the development of a great number of transverse cracks on the compressive side (Fig. 3, Fig. 9). The cracks on the tensile side formed due to the normal tensile stress, which exceeded the strength of the SiC matrix [55][56]. These cracks propagated from the matrix into the fibre bundles, and then arrested. Their development, which increases the compliance of the damaged region, has a small but measurable effect on the effective modulus of the specimen and the position of its neutral axis.

The damage modes on the compressive side are more complex, but similar in both Series 1 and Series 2 composites. Schematic diagrams of the dominant damage at peak load and after failure are shown in Fig. 14. Blue arrows represent the position of the upper loading pin, and red ellipses represent fibre bundles. At the compressive side, the local stress concentration in the region in direct contact with the loading pin resulted in matrix cracking, and the transverse compression caused shear fracture within the nearby fibre bundles. Similar phenomena were observed during 3-point bend flexure testing of 3D five-directional braided composites [45]. This damage is quite localized beneath the loading pin. More significantly, the high longitudinal compressive stress caused debonding of the interfaces between the fibre bundles and matrix, and also within fibre

bundles, such that an increasing number of transverse cracks developed in the damaged fibre bundles with increasing load (Fig. 9). Such debonding damage, also described as delamination, has been observed in an alumina-alumina ceramic-matrix composite [53], SiC/SiC composites [57] and other 3D woven composites [58] under flexural loading. This damage significantly increased the compliance of the compressive region of the specimen. The ultimate failure of both composites resulted from damage that extended from the compressive to the tensile surface, until the specimen became unstable and was unable to sustain the applied flexural stress. Although damage at the tensile surface occurred first, and this corresponded to the onset of nonlinearity of the macroscopic curve, it did not account for the complete loss of the loading capacity of the specimen.

The conditions after failure can be observed more clearly using scanning electric microscopy (SEM). Fig. 15a shows SEM images of the fracture surface of specimen 2-1. Conspicuous fibre pull-out occurred on the tensile side, while no such phenomenon was observed on the compressive side. Moreover, the fracture surfaces of the fibres on the tensile side are perpendicular to the fibre axis direction, while most of the fracture surfaces of the fibres on the compressive side are inclined to the fibre axis direction. These observations indicate that the fibres on the tensile side fractured under tensile loading, while the fibres on the compressive side fail by shearing or buckling. Obvious matrix cracking and interfacial debonding can be observed within fibre bundles on both sides. Fig. 15b shows SEM images of the side surface of specimen 2-3 (the red arrow represents the position of the loading pin). Fracture modes including matrix cracking,

interfacial debonding and fibre breakage all occurred on the compressive side. The observation of cracks on the tensile side is also consistent with the X- CT observations.

The distribution and pattern of damage development, which was indicated by optical surface observations in the Series 1 composite, was verified by in situ X-CT of the Series 2 composite. In both materials, damage initiated first at the tensile surface and was arrested by the braided structure. The maximum flexural stress was limited by compressive failure, which occurred close to the central pin of the three-point loaded specimen. Flexural failure was thus affected by the specimen test method, and flexural strength measured in this manner should not be considered as a material property. This observation in both materials and specimen geometries indicates a common problem for flexural testing of 3D braided ceramic composites.

In the flexural testing of the two composites, both the long span and short span specimens showed similar behaviour. This can be related to the relatively low interfacial debonding strength [59][60]. The interfacial debonding strength can notably influence the flexural properties of SiC/SiC composites, particularly when subject to cyclic loading [61], so it is necessary to pay close attention to this property when preparing this type of composite.

4. Conclusion

Flexural tests of two different 3D braided ceramic fibre composites, with silicon carbide matrices manufactured by PIP with different precursors and types of SiC fibres have

been studied. In situ quantitative study, using image correlation in 2D and/or 3D, provides insight into the sequence of damage processes that lead to failure. The effective elastic modulus can be obtained by analysis of the specimen curvature using image correlation, applied to in situ optical and X-ray tomography images. The change in this modulus provides a measure of the effects of mechanical damage within the microstructure. In both composites, tensile damage occurs first by matrix cracking. However, the ultimate failure of the specimen at the flexural strength occurs after the propagation of a mass of inter- and intra-fibre bundle cracking that initiates in the region of maximum compressive stress close to the loading pin. The flexural strength obtained in such tests is therefore not a material parameter, but can depend on the specimen and test geometry.

Acknowledgements

This work was supported by the National Natural Science Foundation of China [grant numbers 51772009 and 51911530201]. We acknowledge EPSRC Grant EP/M02833X/1 “University of Oxford: experimental equipment upgrade” that supported the Xradia Versa 510 microscope and facilities for data analysis and visualization. The authors want to express their gratitude to Camille Chateau and Michel Bornert from Laboratoire Navier/Ecoles des Ponts ParisTech for the software support relating to image subtraction calculation. The work was conducted at the University of Oxford, with Beihang University support for Liu Changqi as a recognised student. The first and second generation fibres (KD-1 and KD-2) were produced by the

National University of Defense Technology, who also provided the Series 1 specimens. The Series 2 specimens were provided by the School of Physics and Nuclear Energy Engineering of Beihang University

Author Credit

Changqi Liu: Investigation, Methodology, Writing – original draft, **Yang Chen:** Software, Writing – review and editing, **Duoqi Shi:** Conceptualization, Supervision, Funding acquisition, **James Marrow:** Conceptualization, Supervision, Writing – review and editing, **Xin Jing:** Investigation, **Xiaoguang Yang:** Supervision, Project administration.

Data Availability

The raw/processed data required to reproduce these findings cannot be shared at this time due to technical or time limitations

References

[1] Lacombe A, Spriet P, Allaria A, Bouillon E, Habarou G. Ceramic Matrix Composites to make breakthroughs in aircraft engine performance. Collect Tech Pap - AIAA/ASME/ASCE/AHS/ASC Struct Struct Dyn Mater Conf 2009. https://doi.org/10.2514/6.2009-2675.

[2] Morscher GN. Fiber-Reinforced Ceramic Matrix Composites for Aero Engines. Encycl Aerosp Eng 2014:1–10.

https://doi.org/10.1002/9780470686652.eae220.

[3] Bale HA, Haboub A, Macdowell AA, Nasiatka JR, Parkinson DY, Cox BN, et al. Real-time quantitative imaging of failure events in materials under load at temperatures above 1,600°C. Nat Mater 2013;12:40–6. https://doi.org/10.1038/nmat3497.

[4] Naslain R. Design, preparation and properties of non-oxide CMCs for application in engines and nuclear reactors: An overview. Compos Sci Technol 2004;64:155–70. https://doi.org/10.1016/S0266-3538(03)00230-6.

[5] Katoh Y, Snead LL, Henager CH, Nozawa T, Hinoki T, Iveković A, et al. Current status and recent research achievements in SiC/SiC composites. J Nucl Mater 2014;455:387–97. https://doi.org/10.1016/j.jnucmat.2014.06.003.

[6] Zhang C, Curiel-Sosa JL, Bui TQ. Meso-scale progressive damage modeling and life prediction of 3D braided composites under fatigue tension loading. Compos Struct 2018;201:62–71. https://doi.org/10.1016/j.compstruct.2018.06.021.

[7] Chao D, Jiang JJ, Fang LC. Algorithm design of four-step three-dimensional braided composite structures in Matlab environment. Appl Mech Mater 2013;365–366:1144–7. https://doi.org/10.4028/www.scientific.net/AMM.365-366.1144.

[8] Hao W, Yuan Y, Yao X, Ma Y. Computational analysis of fatigue behavior of 3D 4-directional braided composites based on unit cell approach. Adv Eng

Softw 2015;82:38–52. https://doi.org/10.1016/j.advengsoft.2014.12.007.

[9] Bansal NP, Lamon J. Ceramic matrix composites: materials, modeling and technology. John Wiley & Sons; 2014.

[10] F.W.Zok. Ceramic-matrix composites enable revolutionary gains in turbine engine efficiency. Am Ceram Soc Bull 2016;95:22 28.

[11] Lamon J. Chemical vapor infiltrated SiC/SiC composites (CVI SIC/SIC). Handb. Ceram. Compos., Springer; 2005, p. 55–76.

[12] Corman GS, Luthra KL. Silicon melt infiltrated ceramic composites (HiPerComp^{TM}). Handb. Ceram. Compos., Springer; 2005, p. 99–115.

[13] Chen MW, Qiu HP, Jiao J, Li XQ, Wang Y, Zou H. Preparation of high performance SiCf/SiC composites through PIP process. Key Eng. Mater., vol. 544, Trans Tech Publ; 2013, p. 43–7.

[14] Shimoda K, Park JS, Hinoki T, Kohyama A. Influence of pyrolytic carbon interface thickness on microstructure and mechanical properties of SiC/SiC composites by NITE process. Compos Sci Technol 2008;68:98–105. https://doi.org/10.1016/j.compscitech.2007.05.037.

[15] DiCarlo JA, Yun H-M, Morscher GN, Bhatt RT. SiC/SiC composites for 1200 C and above. Handb. Ceram. Compos., Springer; 2005, p. 77–98.

[16] Morscher GN, Pujar V V. Creep and stress-strain behavior after creep for SiC fiber reinforced, melt-infiltrated SiC matrix composites. J Am Ceram Soc 2006;89:1652–8. https://doi.org/10.1111/j.1551-2916.2006.00939.x.

[17] Zou C, Marrow TJ, Reinhard C, Li B, Zhang C, Wang S. Porosity characterization of fiber-reinforced ceramic matrix composite using synchrotron X-ray computed tomography. J Instrum 2016;11. https://doi.org/10.1088/1748-0221/11/03/C03052.

[18] Zhao S, Zhou X, Yu J, Mummery P. Effect of heat treatment on microstructure and mechanical properties of PIP-SiC/SiC composites. Mater Sci Eng A 2013;559:808–11. https://doi.org/10.1016/j.msea.2012.09.027.

[19] Yu HJ, Zhou XG, Zhang W, Peng HX, Zhang CR, Huang ZL. Mechanical properties of 3D KD-I SiCf/SiC composites with engineered fibre-matrix interfaces. Compos Sci Technol 2011;71:699–704. https://doi.org/10.1016/j.compscitech.2011.01.014.

[20] Jing X, Shi D, Yang X, Zhao C. Fiber strength measurement for KD-I(f)/SiC composites and correlation to tensile Mechanical behavior at room and elevated temperatures. Ceram Int 2015;41:299–307. https://doi.org/10.1016/j.ceramint.2014.08.072.

[21] Jing X, Yang X, Shi D, Niu H. Tensile creep behavior of three-dimensional four-step braided SiC/SiC composite at elevated temperature. Ceram Int 2017;43:6721–9. https://doi.org/10.1016/j.ceramint.2017.02.076.

[22] Hou Z, Luo R, Yang W, Xu H, Han T. Effect of fiber directionality on the static and dynamic mechanical properties of 3D SiCf/SiC composites. Mater Sci Eng A 2016;658:263–71. https://doi.org/10.1016/j.msea.2016.02.006.

[23] Zhang XH, Gao HS, Wen ZX, Li MY, Zhou XG, Yue ZF. Effect of film cooling holes on the mechanical properties of 3D braided SiCf/SiC composites at 1350 °C in air. Ceram Int 2020;46:7982–90. https://doi.org/10.1016/j.ceramint.2019.12.020.

[24] Rajan VP, Rossol MN, Zok FW. Optimization of Digital Image Correlation for High-Resolution Strain Mapping of Ceramic Composites. Exp Mech 2012;52:1407–21. https://doi.org/10.1007/s11340-012-9617-1.

[25] Yu L, Pan B. Experimental study of tensile properties and deformation evolutions of 2D and 2.5D woven SiO2f/SiO2 composites using single-camera stereo-digital image correlation. Compos Struct 2018;200:589–98. https://doi.org/10.1016/j.compstruct.2018.05.135.

[26] Dong Y, Shi X, Zhang Z, Pan B. In-situ bending behavior and failure characterization of 3D needle-punched C/SiC composites. Mater Today Commun 2017;13:378–85. https://doi.org/10.1016/j.mtcomm.2017.11.002.

[27] Teng X, Shi D, Cheng Z, Jing X, Lyu S, Yang X. Investigation on non-uniform strains of a 2.5D woven ceramic matrix composite under in-plane tensile stress. J Eur Ceram Soc 2020;40:36–48. https://doi.org/10.1016/j.jeurceramsoc.2019.08.030.

[28] Meyer P, Waas AM. Experimental results on the elevated temperature tensile response of SiC/SiC ceramic matrix notched composites. Compos Part B Eng 2018;143:269–81. https://doi.org/10.1016/j.compositesb.2018.01.019.

[29] Zhang D, Meyer P, Waas AM. An experimentally validated computational model for progressive damage analysis of notched oxide/oxide woven ceramic matrix composites. Compos Struct 2017;161:264–74. https://doi.org/10.1016/j.compstruct.2016.11.001.

[30] Bernachy-Barbe F, Gélébart L, Bornert M, Crépin J, Sauder C. Characterization of SiC/SiC composites damage mechanisms using Digital Image Correlation at the tow scale. Compos Part A Appl Sci Manuf 2015;68:101–9. https://doi.org/10.1016/j.compositesa.2014.09.021.

[31] Gao Y, Wang Y, Yang X, Liu M, Xia H, Huai P, et al. Synchrotron X-ray tomographic characterization of CVI engineered 2D-woven and 3D-braided SiCf/SiC composites. Ceram Int 2016;42:17137–47. https://doi.org/10.1016/j.ceramint.2016.08.001.

[32] Blackshire JL, Medina E, Na J, Evaluation UN. Nondestructive Evaluation of Microstructure in 2011;1:13–21.

[33] Morales-Rodríguez A, Reynaud P, Fantozzi G, Adrien J, Maire E. Porosity analysis of long-fiber-reinforced ceramic matrix composites using X-ray tomography. Scr Mater 2009;60:388–90. https://doi.org/10.1016/j.scriptamat.2008.11.018.

[34] Chen Y, Gélébart L, Chateau C, Bornert M, Sauder C, King A. Analysis of the damage initiation in a SiC/SiC composite tube from a direct comparison between large-scale numerical simulation and synchrotron X-ray micro-

computed tomography. Int J Solids Struct 2019;161:111–26. https://doi.org/10.1016/j.ijsolstr.2018.11.009.

[35] Chen Y, Gélébart L, Chateau C, Bornert M, King A, Sauder C, et al. Crack initiation and propagation in braided SiC/SiC composite tubes: Effect of braiding angle. J Eur Ceram Soc 2020. https://doi.org/10.1016/j.jeurceramsoc.2020.04.060.

[36] Wan F, Liu R, Wang Y, Cao Y, Zhang C, Marrow TJ. In situ observation of compression damage in a 3D needled-punched carbon fiber-silicon carbide ceramic matrix composite. Compos Struct 2019;210:189–201. https://doi.org/10.1016/j.compstruct.2018.11.041.

[37] Xue Y, Wang Q, Hu J, Zhou H, Shan Q, Zhu G, et al. Acoustic emission and X-ray computed microtomography characterization of damage accumulation in a woven Cf/SiC composite. Mater Charact 2019;155:109748. https://doi.org/10.1016/j.matchar.2019.05.033.

[38] Maillet E, Singhal A, Hilmas A, Gao Y, Zhou Y, Henson G, et al. Combining in-situ synchrotron X-ray microtomography and acoustic emission to characterize damage evolution in ceramic matrix composites. J Eur Ceram Soc 2019;39:3546–56. https://doi.org/10.1016/j.jeurceramsoc.2019.05.027.

[39] Quiney Z, Weston E, Ian Nicholson P, Pattison S, Bache MR. Volumetric assessment of fatigue damage in a SiCf/SiC ceramic matrix composite via in situ X-ray computed tomography. J Eur Ceram Soc 2020:0–1.

https://doi.org/10.1016/j.jeurceramsoc.2020.04.037.

[40] Marrow J, Reinhard C, Vertyagina Y, Saucedo-Mora L, Collins D, Mostafavi M. 3D Studies of Damage by Combined X-ray Tomography and Digital Volume Correlation. Procedia Mater Sci 2014;3:1554–9. https://doi.org/10.1016/j.mspro.2014.06.251.

[41] Mazars V, Caty O, Couégnat G, Bouterf A, Roux S, Denneulin S, et al. Damage investigation and modeling of 3D woven ceramic matrix composites from X-ray tomography in-situ tensile tests. Acta Mater 2017;140:130–9. https://doi.org/10.1016/j.actamat.2017.08.034.

[42] Chateau C, Nguyen TT, Bornert M, Yvonnet J. DVC-based image subtraction to detect microcracking in lightweight concrete. Strain 2018;54:1–18. https://doi.org/10.1111/str.12276.

[43] Whitlow T, Jones E, Przybyla C. In-situ damage monitoring of a SiC/SiC ceramic matrix composite using acoustic emission and digital image correlation. Compos Struct 2016;158:245–51. https://doi.org/10.1016/j.compstruct.2016.09.040.

[44] Croom BP, Xu P, Lahoda EJ, Deck CP, Li X. Quantifying the three-dimensional damage and stress redistribution mechanisms of braided SiC/SiC composites by in situ volumetric digital image correlation. Scr Mater 2017;130:238–41. https://doi.org/10.1016/j.scriptamat.2016.12.021.

[45] Zhang P fei, Zhou W, Yin H fei, Shang Y jing. Progressive damage analysis of

three-dimensional braided composites under flexural load by micro-CT and acoustic emission. Compos Struct 2019;226:111196. https://doi.org/10.1016/j.compstruct.2019.111196.

[46] Wan F, Liu R, Wang Y, Cao Y, Zhang C, Marrow TJ. Damage development during flexural loading of a 5-directional braided C/C-SiC composite, characterized by X-ray tomography and digital volume correlation. Ceram Int 2019;45:5601–12. https://doi.org/10.1016/j.ceramint.2018.12.020.

[47] Wang P, Liu F, Wang H, Li H, Gou Y. A review of third generation SiC fibers and SiCf/SiC composites. J Mater Sci Technol 2019;35:2743–50. https://doi.org/10.1016/j.jmst.2019.07.020.

[48] Li M, Zhou X, Yang H, Wang H, Yu J. Mechanical properties of the SiC f /SiC composites reinforced with KD-I and KD-II fibers fabricated assisted by a microwave heating method. Ceram Int 2019;45:12957–64. https://doi.org/10.1016/j.ceramint.2019.03.223.

[49] ASTM International. ASTM C1341-13 - Standard Test Method for Flexural Properties of Continuous Fiber-Reinforced Advanced Ceramic Composites. ASTM Int 2013;i:1–21. https://doi.org/10.1520/C1341-13.2.

[50] BS EN 15156. Advanced technical ceramics — Mechanical properties of ceramic composites at room temperature — Determination of fatigue properties at constant amplitude. Br Stand Institute, UK 2006;3.

[51] Jing X. Investigation on High Temperature Mechanical Behaviour of Three-

dimensional Braided Ceramic Matrix Composites [Ph.D. Thesis]. Beihang University, China, 2016.

[52] Hao Z, Ji X, Deng L, Ke H, Liu L. Measurement of multiple mechanical properties for polymer composites using digital image correlation at elevated temperatures. Mater Des 2021;198. https://doi.org/10.1016/j.matdes.2020.109349.

[53] Pirzada TJ, Liu D, Ell J, Barnard H, Šulák I, Galano M, et al. In situ observation of the deformation and fracture of an alumina-alumina ceramic-matrix composite at elevated temperature using x-ray computed tomography. J Eur Ceram Soc 2021. https://doi.org/10.1016/j.jeurceramsoc.2021.01.030.

[54] Yang H, Zhou X, Yu J, Wang H, Huang Z. Effect of microwave sintering time on the flexural properties of the SiC/SiC composites. Ceram Int 2015;41:14692–7. https://doi.org/10.1016/j.ceramint.2015.07.192.

[55] Xin J, Zhen C, Xuefeng T, Xiaoguang Y, Duoqi S. Reconstruction of meso-structure and numerical simulations of the mechanical behavior of three-dimensional four-directional braided ceramic matrix composites. Ceram Int 2020. https://doi.org/10.1016/j.ceramint.2020.08.107.

[56] Shen X, Li M, Dai Y, Zhou X, He P. The effects of preparation temperature on the SiCf/SiC 3D4d woven composite. Ceram Int 2020;46:13088–94. https://doi.org/https://doi.org/10.1016/j.ceramint.2020.02.080.

[57] Patel A, Sato E, Takagi T, Shichijo N. Bending fatigue behavior in an advanced

SiC/SiC ceramic matrix composite component at elevated temperature in air. Compos Part C Open Access 2021;5:100127. https://doi.org/10.1016/j.jcomc.2021.100127.

[58] Dai S, Cunningham PR, Marshall S, Silva C. Influence of fibre architecture on the tensile, compressive and flexural behaviour of 3D woven composites. Compos Part A Appl Sci Manuf 2015;69:195–207. https://doi.org/10.1016/j.compositesa.2014.11.012.

[59] Zhao S, Zhou X, Yu J, Mummery P. Mechanical properties and in situ crack growth observation of SiC/SiC composites. Ceram Int 2014;40:7481–5. https://doi.org/10.1016/j.ceramint.2013.12.098.

[60] Hou Z, Luo R, Yang W, Xu H, Han T. Effect of interface type on the static and dynamic mechanical properties of 3D braided SiCf/SiC composites. Mater Sci Eng A 2016;669:66–74. https://doi.org/10.1016/j.msea.2016.05.080.

[61] Rouby D, Reynaud P. Fatigue behaviour related to interface modification during load cycling in ceramic-matrix fibre composites. Compos Sci Technol 1993;48:109–18. https://doi.org/10.1016/0266-3538(93)90126-2.

Figures Captions

Fig. 1 Experimental setup for: a) flexural tests with DIC; b) flexural tests with in situ X-CT

Fig. 2 a) Nominal stress vs strain curves of four Series 1 specimens (1-1–1-4) (the curves of different span to thickness ratios are presented as solid lines and dash dot lines respectively); b) optical images of four Series 1 specimens (1-1–1-4) captured at their peak loads.

Fig. 3 a) The nominal tensile stress-strain curve of specimen 1-1 (points a, b, c, d correspond to the start of the nonlinear stage, the occurrence of the interlayer debonding, the peak load and the post-failure condition); Example optical images recorded during flexural testing of Series 1 specimen 1-1 at increasing flexural stress: b) tensile cracking (450 MPa); c) interlayer debonding near the upper compressive surface (613 MPa); d) surface extrusion and buckling near the compressive surface (648 MPa); e) propagation of interlayer debonding to the lower tensile surface (after failure at 593 MPa).

Fig. 4 Evolution of the *Y*-direction displacement fields with increasing load: a) 100 MPa to f) 643 MPa for Series 1 specimen 1-1.

Fig. 5 Evolution of the ε_{XX} strain field with increasing load: a)-f); g) the positions of the neutral axis at different loads (averages of positions where $\varepsilon_{XX} = 0$, measured between $X = 3.1$ mm and $X = 7.1$ mm)

Fig. 6 a) Normalized strains ($\varepsilon_{XX}\frac{I}{M}$) along the direction of thickness (*Y*) for Series 1 specimen 1-1; b) elastic modulus calculated for specimens 1-1 and 1-2, using DIC and the gradient or secant of the stress-strain relationship obtained via the load vs cross-head displacement data ('Experimental curve').

Fig. 7 Cross-head displacement vs load data for the flexural tests of the Series 2 composite. Specimens 2-1 and 2-2 were loaded continuously, and specimens 2-3 and 2-4 were tested with interrupted loading for in situ examination by X-CT at the numbered points (scanning steps).

Fig. 8 a) 3D reconstruction of Series 2 specimen 2-3, imaged by X-CT at step 4 (1033 N, after peak load). Cracks are indicated with red arrows; 2D slices through this volume are shown in b) *XY* and c) *XZ* planes, which are labelled as red and green respectively in a)

Fig. 9 2D slices of Series 2 specimen 2-3, imaged by X-CT at increasing loads to failure (steps 0 to 4): a) vertical *XY* slices; b) horizontal *XZ* slices close to the tensile surface (the position of the loading pin is marked by a black dashed line). The arrows identify the development of damage – see text for details.

Fig. 10 Displacement fields (mm) of Series 2 specimen 2-3 in three directions, measured by DVC of X-CT images, at: a) 1100 N (step 1) and b) at peak load (step 3, 1447 N)

Fig. 11 Comparison of: a) 3D maximum principal strain fields at different loads, and b) visualizations from image subtraction at corresponding loads (steps 1 to 4, Series 2 specimen 2-3); c) image subtraction visualisation for Series 2 specimen 2-4 after failure (step 3)

Fig. 12 The fields of normalized strain ($\varepsilon_{XX} I/M \cdot 10^9$) at X-CT scanning steps 1 to 4, averaged across specimen thickness (Z).

Fig. 13 a) Normalized strains ($\varepsilon_{XX} \frac{I}{M}$) along the direction of thickness (Y) for Series 2 specimen 2-3; b) Effective elastic modulus, obtained by DVC analysis of the strain gradient, and the volume fraction of cracks for Series 2 specimens 2-3 and 2-4 at each X-CT scanning step.

Fig. 14 Schematic diagrams of various damage modes at peak load and after failure

Fig. 15 SEM images of the Series 2 composite: a) the fracture surface of specimen 2-1; b) the side surface of specimen 2-3 (the red arrow represents the position of the loading pin)

Tables

Table 1 Main parameters with respect to the two batches of specimens

	Diameter of fibres /μm	Elastic modulus (fibres) /GPa	Tensile Strength (fibres) /GPa	Matrix precursor	Density (composite) /g/cm^3	Braided angle/°
Series 1	~ 12.5	170-180	1.8-2.0	LPVCS	~ 2.16	~ 25
Series 2	~ 10-12	250-270	2.5-2.7	PCS/xylene	~ 2.09	~ 25

Table 2 Experimental conditions and measured mechanical properties of Series 1 specimens

Specimen	Span to thickness ratio	Elastic modulus /GPa	Flexural strength /MPa
1-1	20	91.9 ± 0.8	650
1-2		78.2 ± 0.5	563
1-3	16	73.4 ± 0.3	412
1-4		80.0 ± 0.5	521

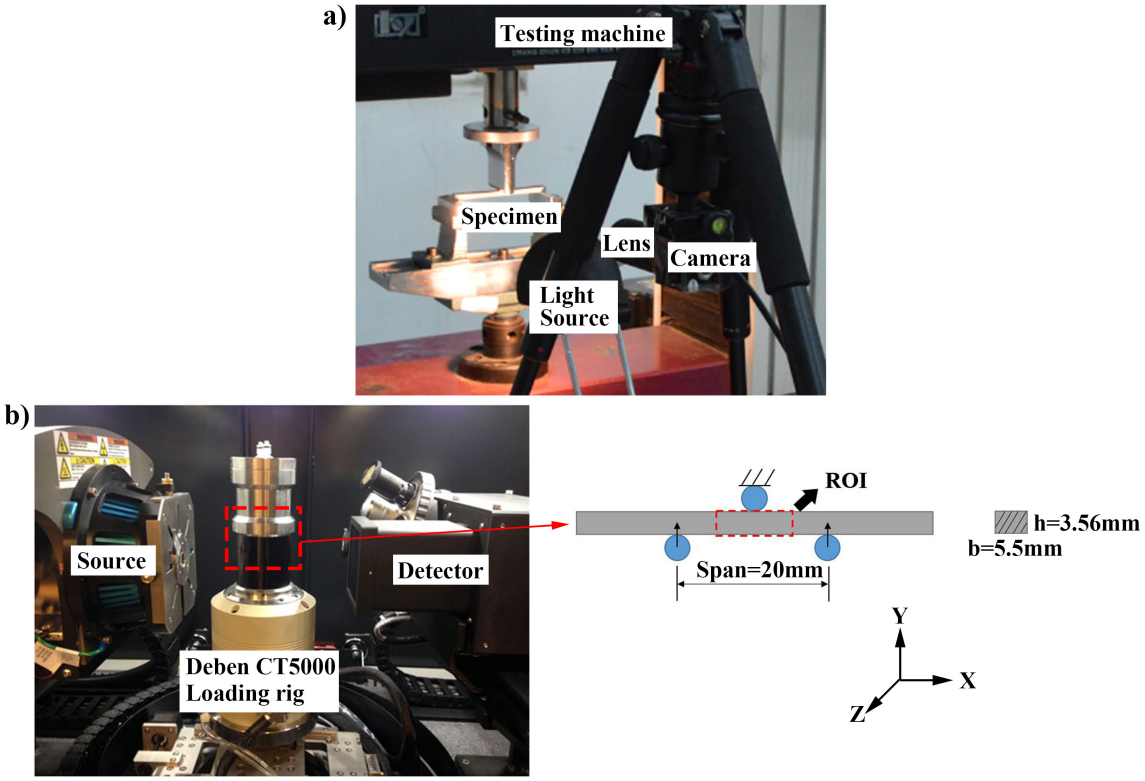
a)
Testing machine
Specimen
Lens
Camera
Light Source
b)
Source
Detector
Deben CT5000 Loading rig
ROI
h=3.56mm
b=5.5mm
Span=20mm
Y
X
Z

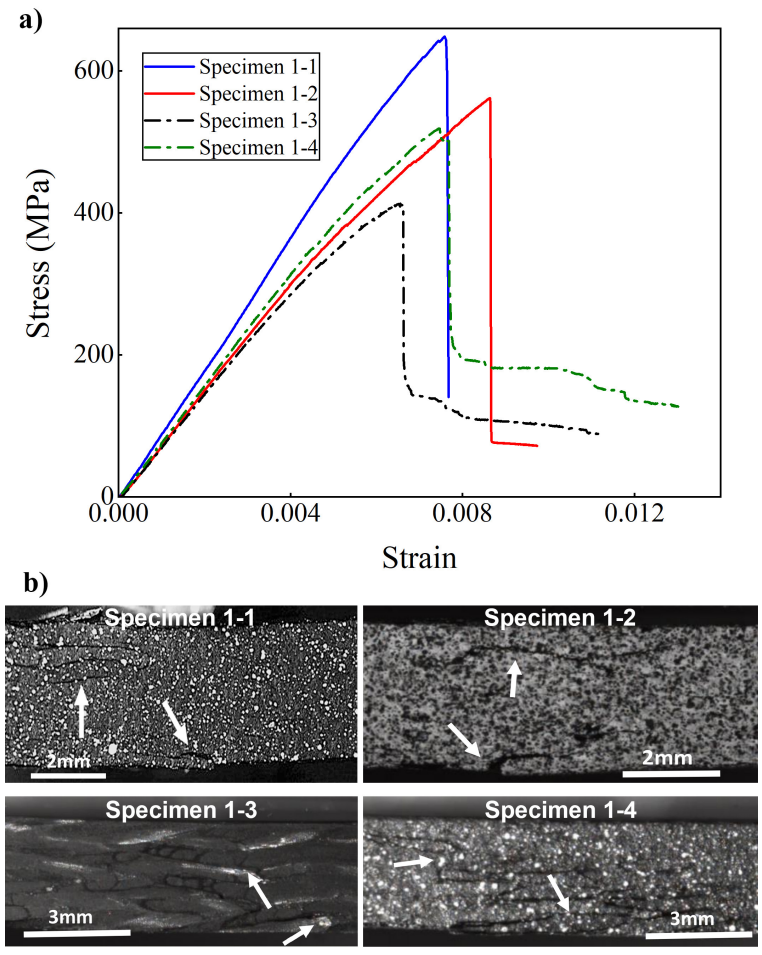
a)
Specimen 1-1
Specimen 1-2
Specimen 1-3
Specimen 1-4
Stress (MPa)
600
400
200
0
0.000
0.004
0.008
0.012
Strain
b)
Specimen 1-1
2mm
Specimen 1-2
2mm
Specimen 1-3
3mm
Specimen 1-4
3mm

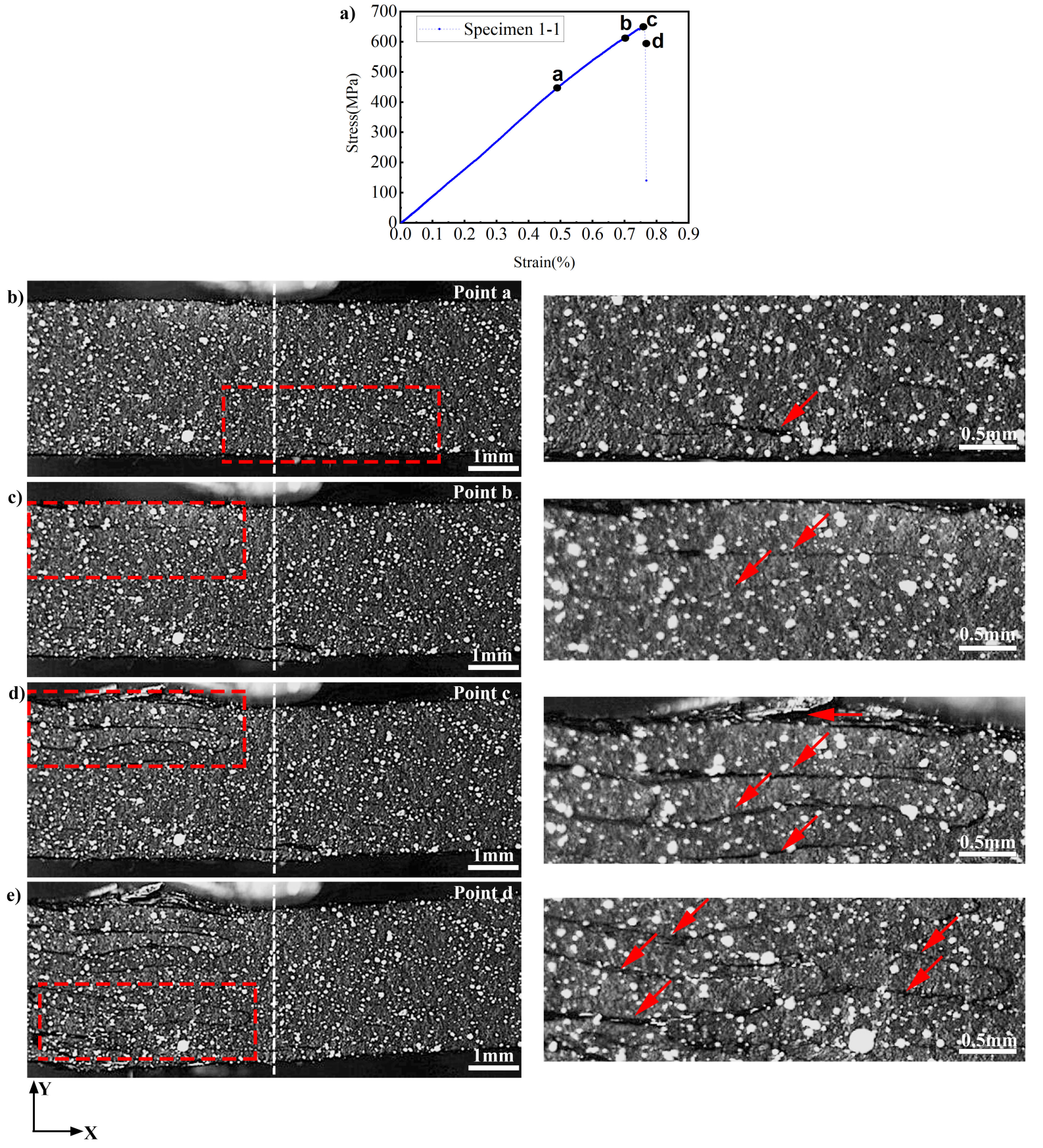
a)
Specimen 1-1
Stress(MPa)
Strain(%)
a
b
c
d
b)
Point a
c)
Point b
d)
Point c
e)
Point d
1mm
0.5mm
Y
X

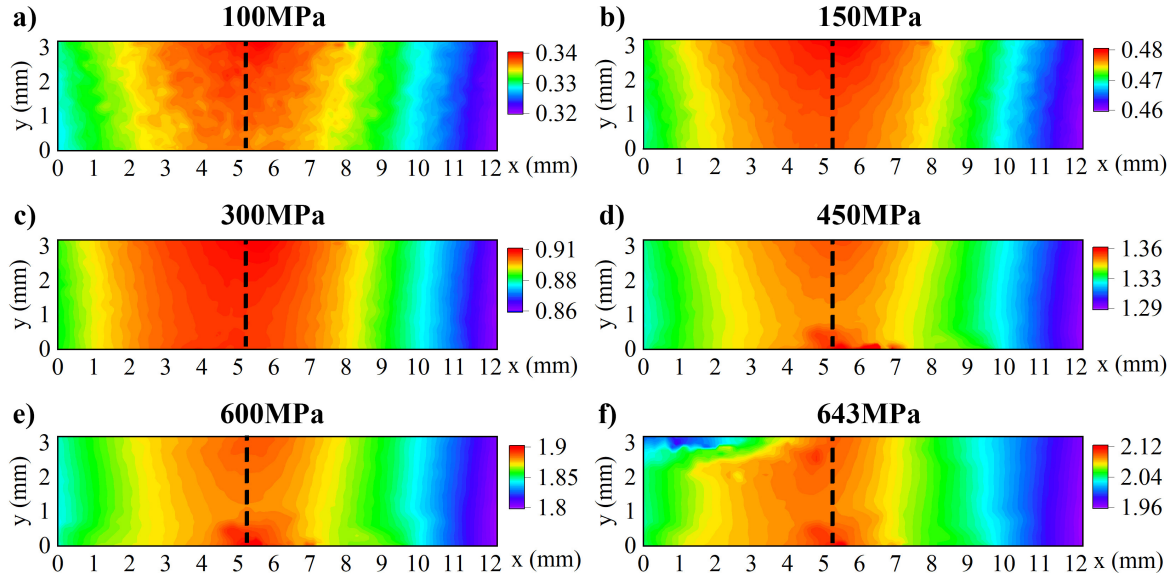
a)
100MPa
b)
150MPa
c)
300MPa
d)
450MPa
e)
600MPa
f)
643MPa
y (mm)
x (mm)
0.34
0.33
0.32
0.48
0.47
0.46
0.91
0.88
0.86
1.36
1.33
1.29
1.9
1.85
1.8
2.12
2.04
1.96

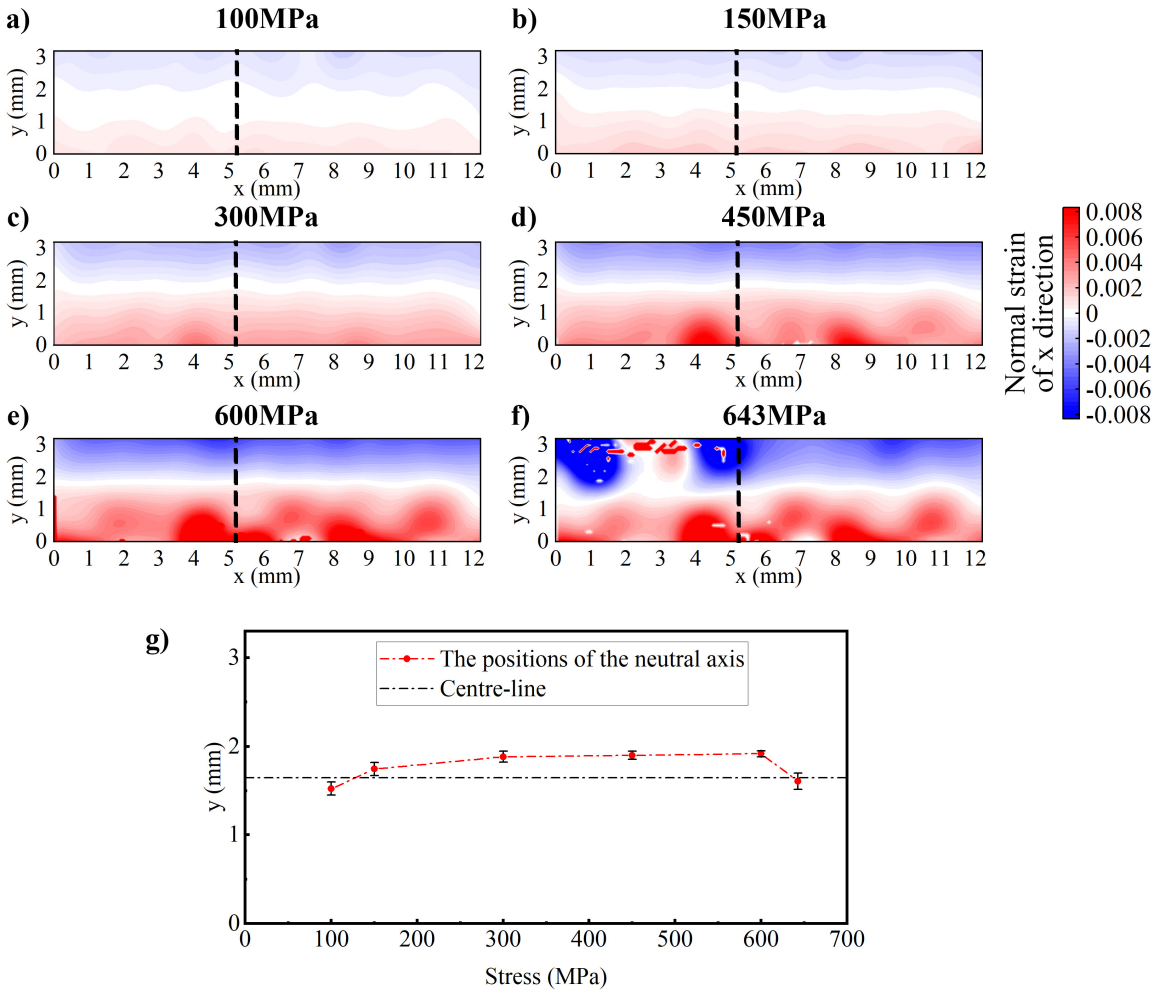
a)
100MPa
b)
150MPa
c)
300MPa
d)
450MPa
e)
600MPa
f)
643MPa
y (mm)
x (mm)
Normal strain of x direction
0.008
0.006
0.004
0.002
0
-0.002
-0.004
-0.006
-0.008
g)
The positions of the neutral axis
Centre-line
y (mm)
Stress (MPa)

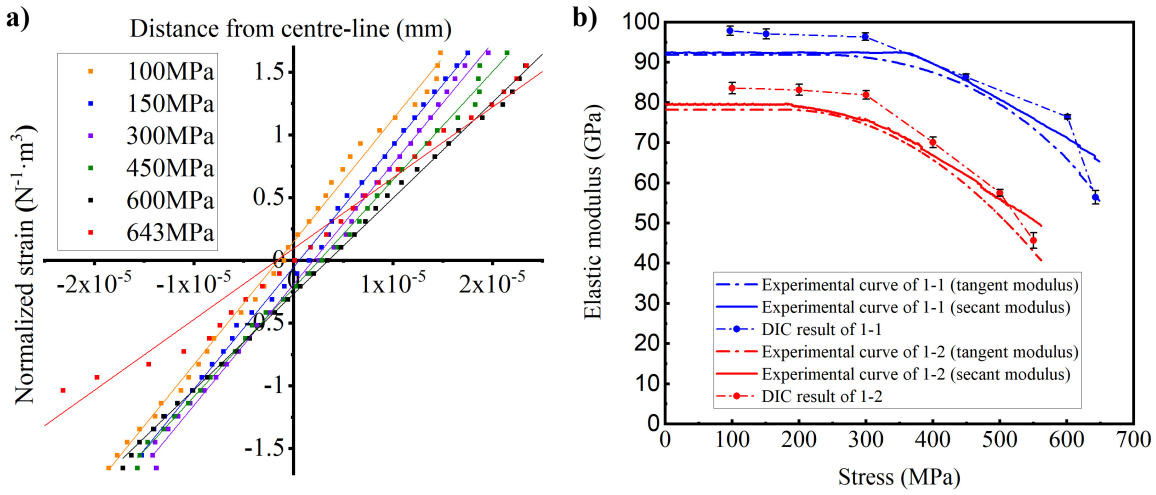
a)
Distance from centre-line (mm)
Normalized strain (N-1·m3)
100MPa
150MPa
300MPa
450MPa
600MPa
643MPa
1.5
1
0.5
0
-0.5
-1
-1.5
-2x10-5
-1x10-5
1x10-5
2x10-5
b)
Elastic modulus (GPa)
Stress (MPa)
Experimental curve of 1-1 (tangent modulus)
Experimental curve of 1-1 (secant modulus)
DIC result of 1-1
Experimental curve of 1-2 (tangent modulus)
Experimental curve of 1-2 (secant modulus)
DIC result of 1-2
0
10
20
30
40
50
60
70
80
90
100
0
100
200
300
400
500
600
700

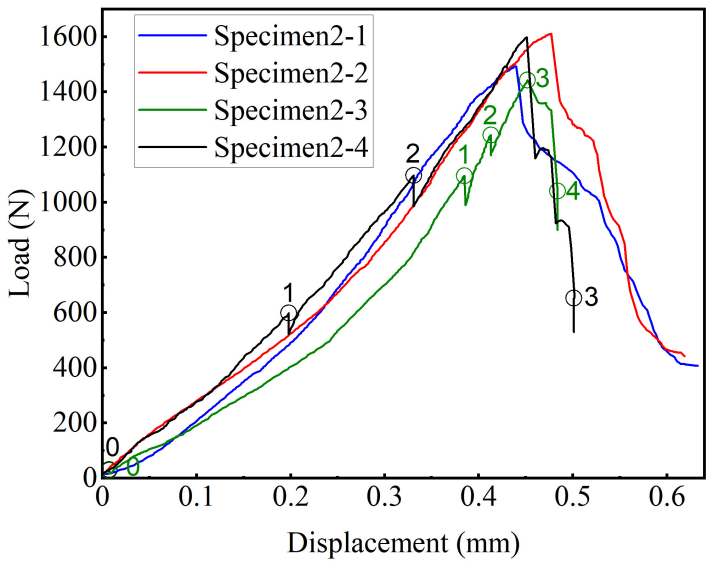
Specimen2-1
Specimen2-2
Specimen2-3
Specimen2-4
Load (N)
Displacement (mm)
0
200
400
600
800
1000
1200
1400
1600
0
0.1
0.2
0.3
0.4
0.5
0.6
0
1
2
3
0
1
2
3
4

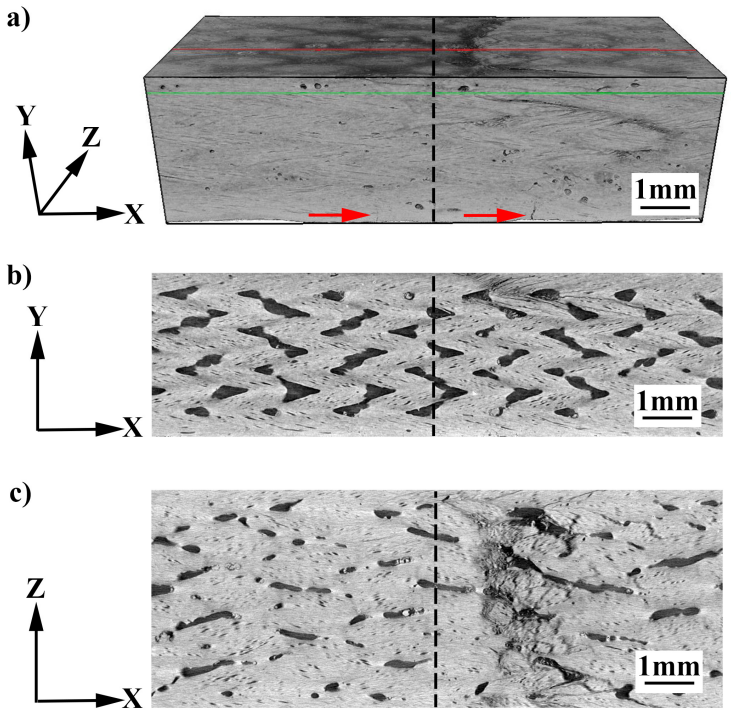
a)
Y
Z
X
1mm
b)
Y
X
1mm
c)
Z
X
1mm

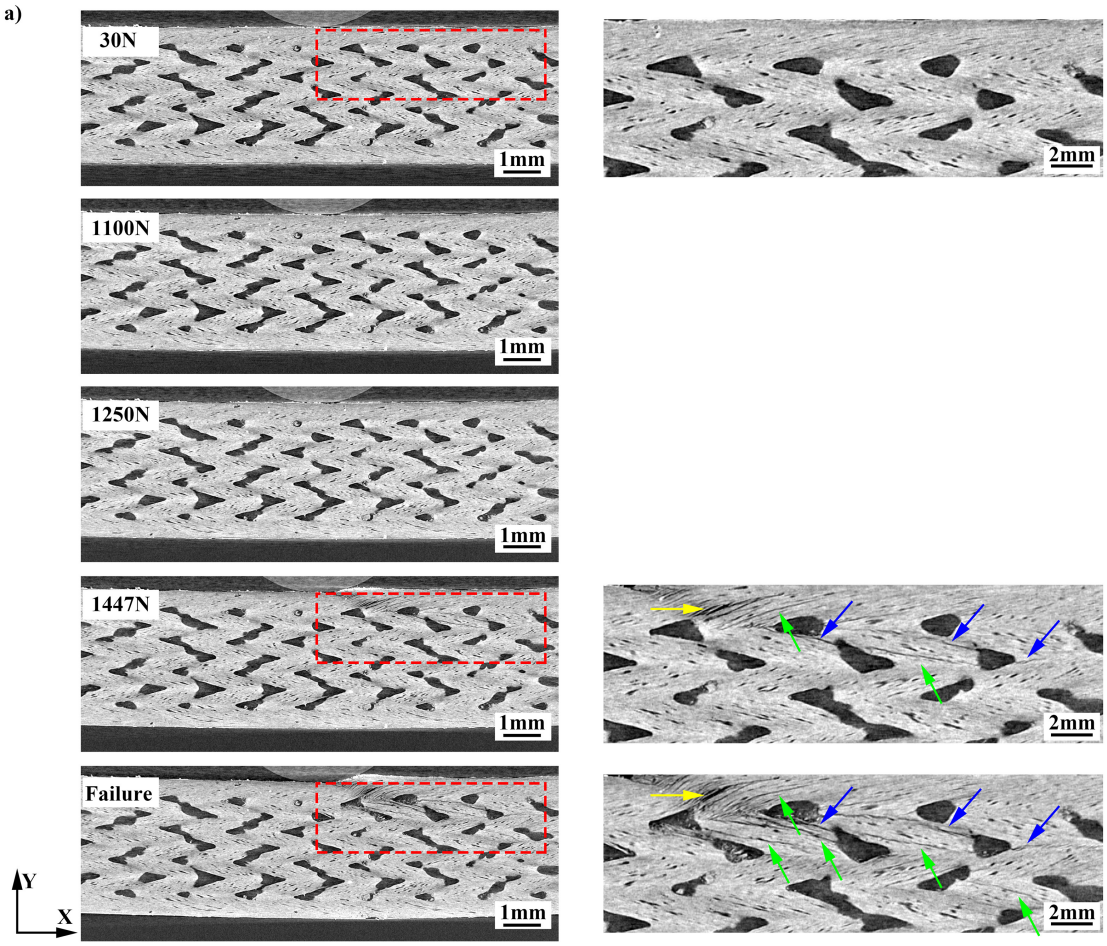
a)
30N
1mm
2mm
1100N
1mm
1250N
1mm
1447N
1mm
2mm
Failure
1mm
2mm
Y
X

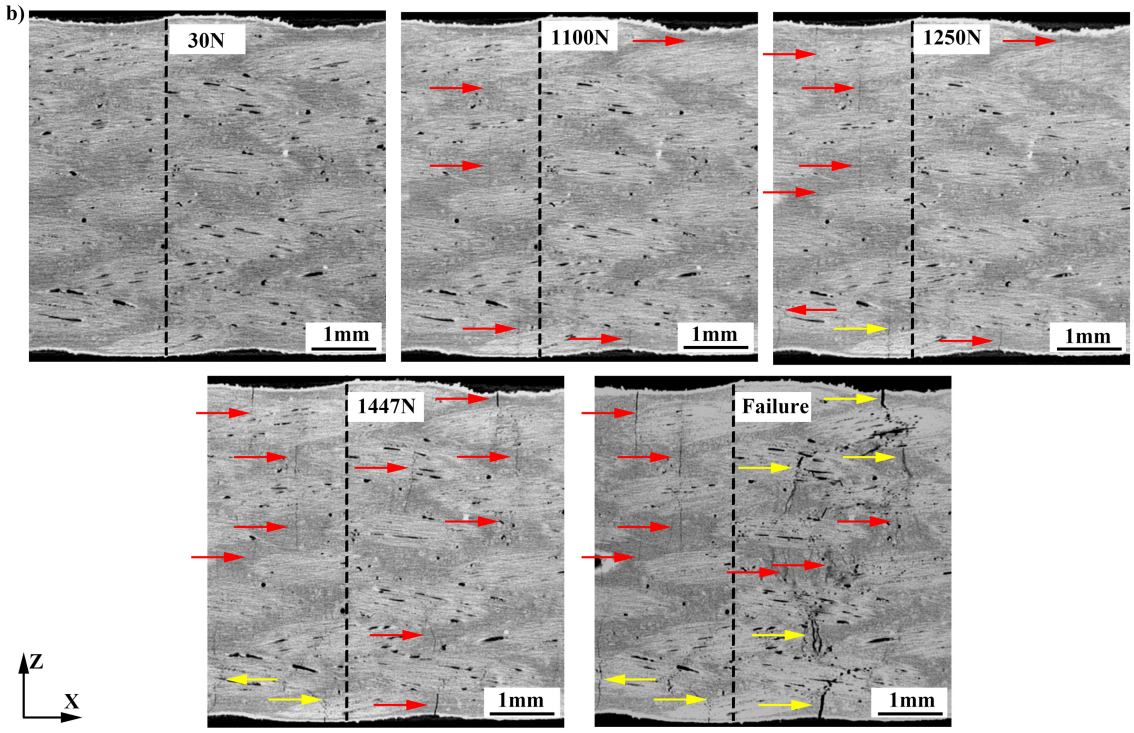
b)
30N
1mm
1100N
1mm
1250N
1mm
1447N
1mm
Failure
1mm
Z
X

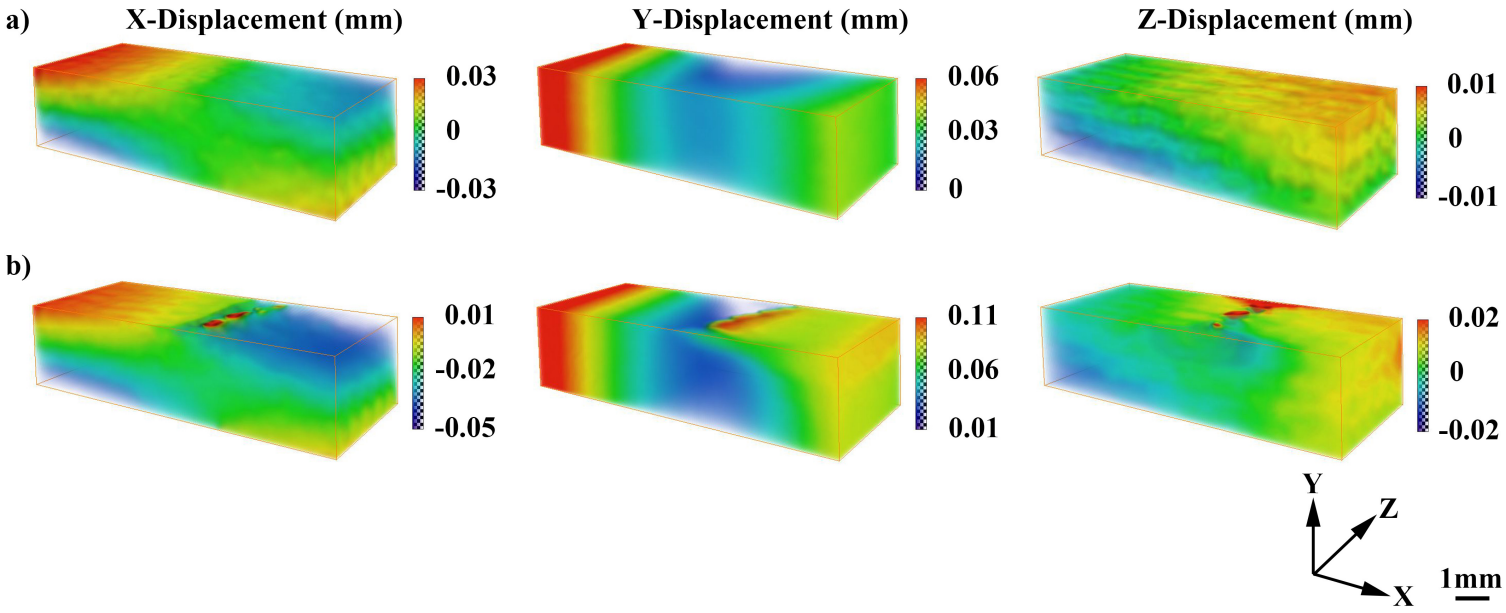
a)
X-Displacement (mm)
Y-Displacement (mm)
Z-Displacement (mm)
0.03
0
-0.03
0.06
0.03
0
0.01
0
-0.01
b)
0.01
-0.02
-0.05
0.11
0.06
0.01
0.02
0
-0.02
Y
Z
X
1mm

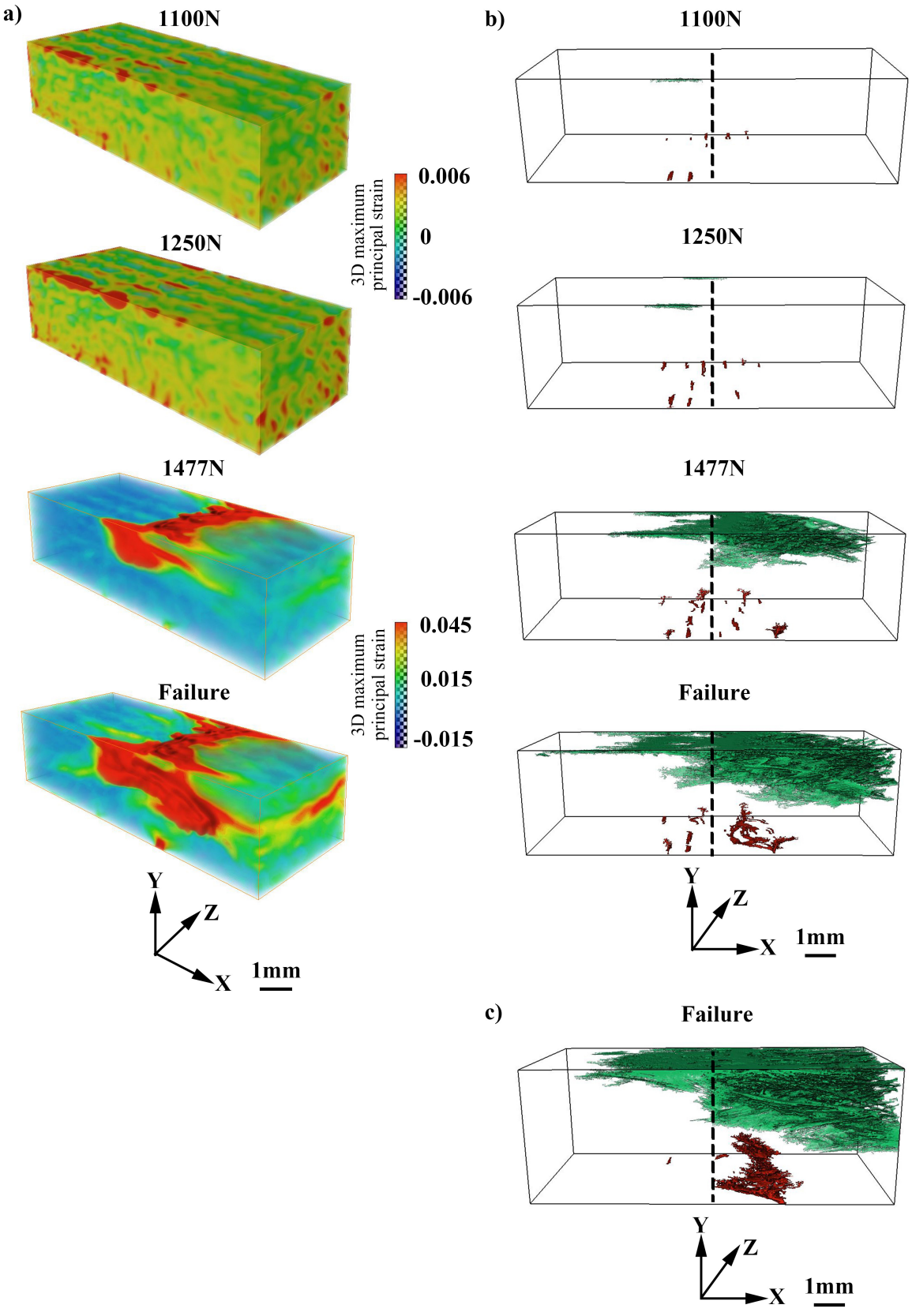
a)
1100N
1250N
1477N
Failure
3D maximum principal strain
0.006
0
-0.006
3D maximum principal strain
0.045
0.015
-0.015
Y
Z
X
1mm
b)
1100N
1250N
1477N
Failure
Y
Z
X
1mm
c)
Failure
Y
Z
X
1mm

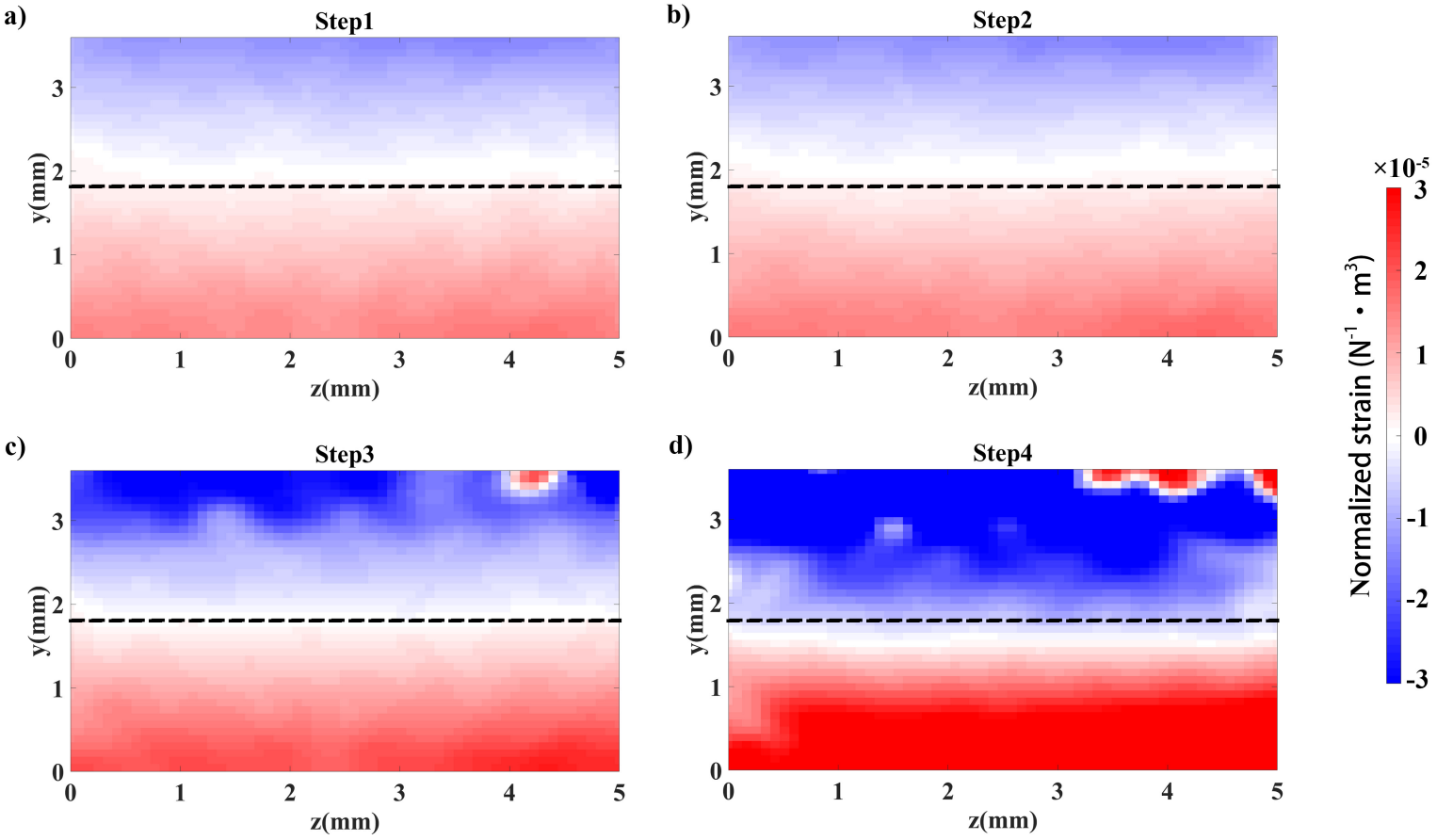
a)
Step1
b)
Step2
c)
Step3
d)
Step4
y(mm)
z(mm)
0
1
2
3
4
5
×10-5
Normalized strain (N-1 • m3)
3
2
1
0
-1
-2
-3

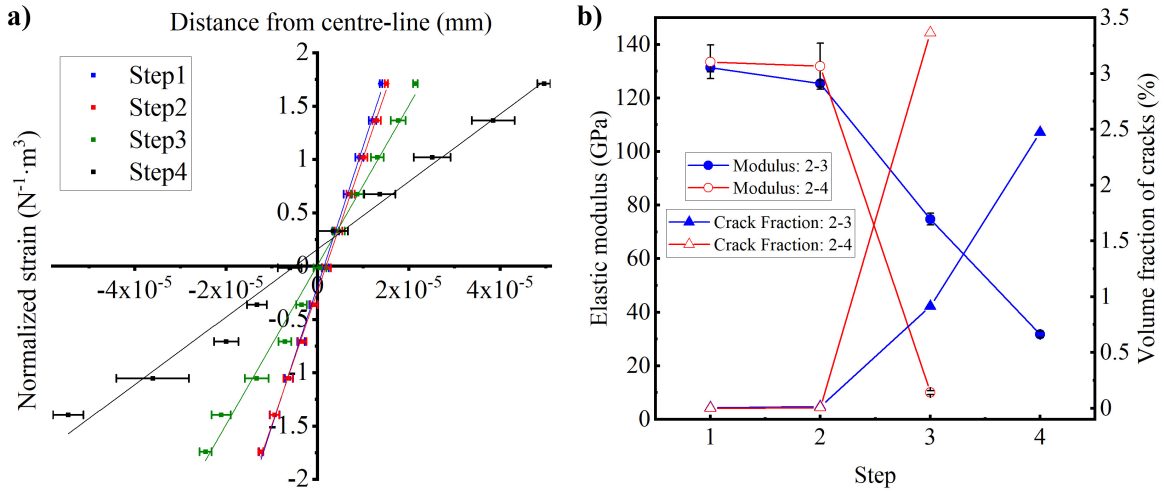
a)
Distance from centre-line (mm)
Normalized strain (N-1·m3)
Step1
Step2
Step3
Step4
2
1.5
1
0.5
0
-0.5
-1
-1.5
-2
-4x10-5
-2x10-5
2x10-5
4x10-5
b)
Elastic modulus (GPa)
Volume fraction of cracks (%)
Step
Modulus: 2-3
Modulus: 2-4
Crack Fraction: 2-3
Crack Fraction: 2-4
140
120
100
80
60
40
20
0
3.5
3
2.5
2
1.5
1
0.5
0
1
2
3
4

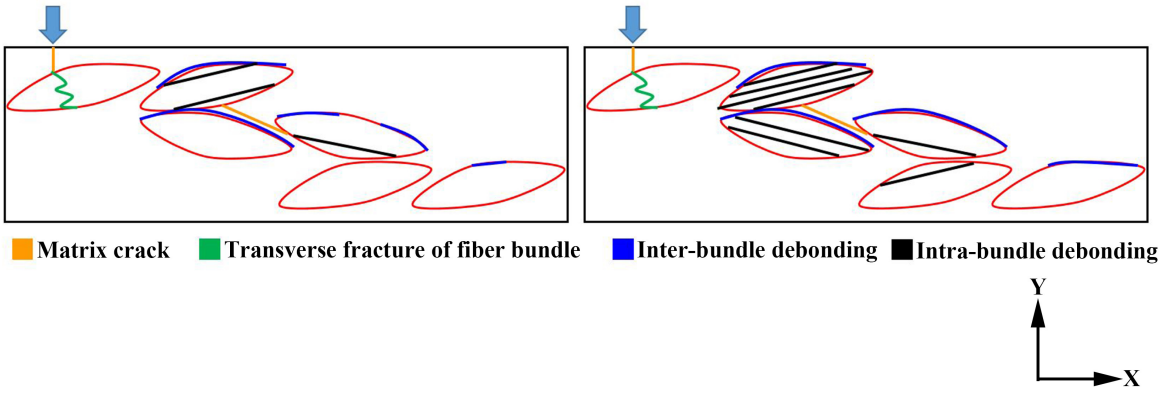
Matrix crack
Transverse fracture of fiber bundle
Inter-bundle debonding
Intra-bundle debonding
Y
X

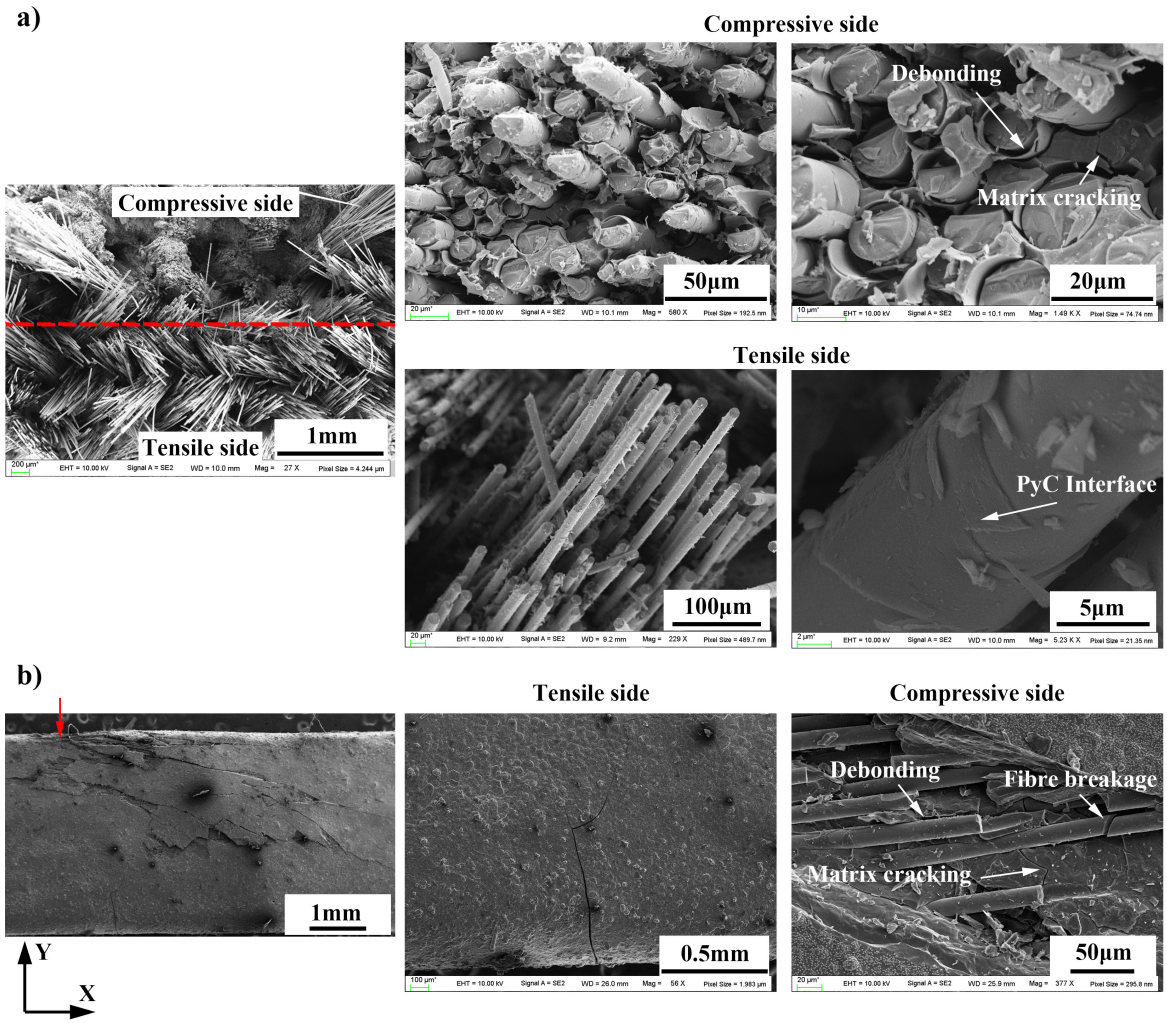
a)
Compressive side
Compressive side
Tensile side
1mm
50µm
Debonding
Matrix cracking
20µm
Tensile side
100µm
PyC Interface
5µm
b)
1mm
Y
X
Tensile side
0.5mm
Compressive side
Debonding
Fibre breakage
Matrix cracking
50µm

Porosity Characterization

X-CT images at the pre-load of 30 N were used to calculate the total porosity, observe the pores structure and study the pores distribution. Due to the different density and chemistry, the gray levels of different constituents due to X-ray attenuation vary in the reconstruction within the range of 0-255. Pores with relatively low gray levels can be separated from other solid phases by applying a contrast threshold, in this case using tools in the Avizo software. The effect of this threshold on the total measured porosity is shown in Fig. 1a. There is a region with low threshold sensitivity within the range between 115-125, and a threshold of 120 was chosen to extract the visible pores. Fig. 1b shows a binary image obtained through this threshold operation.

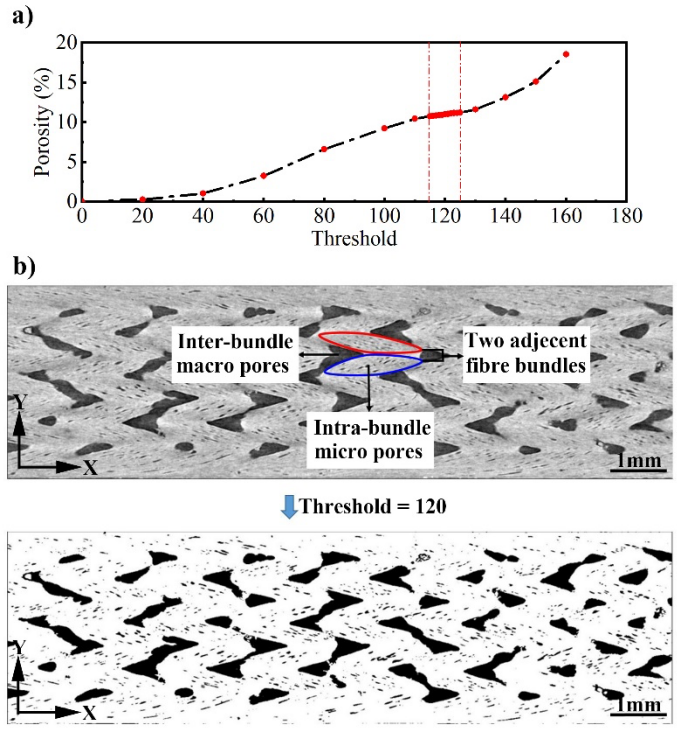

Fig. 1 The process of pore segmentation: a) effect of greyscale threshold [image range 0-255] on total measured porosity; b) segmentation result of an *XY* slice at a threshold of 120.

Fig. 2 provides 3D visualization with respect to structure and distribution of pores. The total porosity fraction (10.89%) was calculated from the volume of all pores, relative to the total volume. Fig. 1b and Fig. 2a show two types of pores, inter-bundle macro pores and intra-bundle micro pores. Macro pores are mostly connected, though some isolated macro pores (i.e. no visible connection) can also be identified (Fig. 2b). The micro pores (Fig. 2c) were obtained by subtracting the image of the macro pores from that of all pores. Micro pores have high aspect ratio and are mostly parallel to the axial direction of fibres. Fig. 2d shows the 3D morphology of pores together with the solid phases. It is difficult to reliably segment the micro pores within the fibre bundles due to limited image resolution. However, the micro pores account for only a minority of total porosity, about 1.66%. Therefore, the measurement of the total porosity is considered reliable.

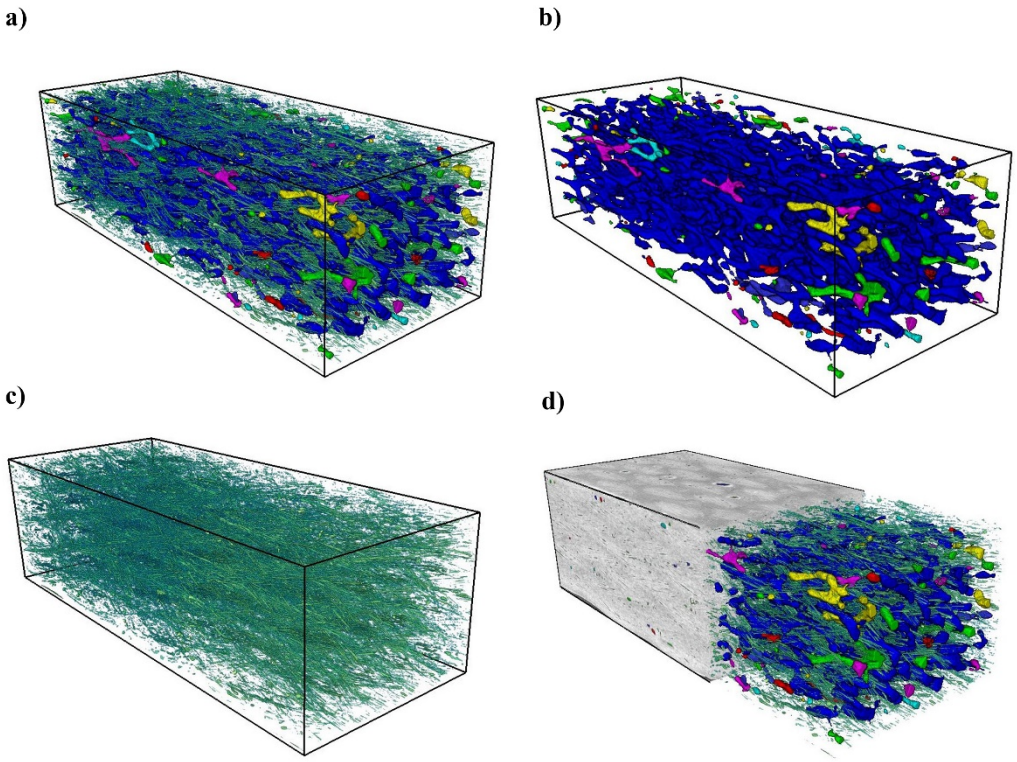

Fig. 2 3D visualization of pores: a) total pores; b)macro pores; c)micro pores; d)with fibre undles and matrix (BUAA Composite, Specimen 2-3)

Area fraction profiles to assess the variation of total pores, macro pores and micro pores as a function of the slice number in the three directions (*XY*, *XZ* and *YZ* slices) are shown in Fig. 3. The total porosity and macro porosity exhibit a significant periodic fluctuation in the *XY* and *XZ* slices, related to the mesoscopic braided structure of the specimen. It is notable that the porosity is quite low near the sample surfaces. In the *YZ* slices (i.e. along the specimen length), the porosity fluctuates aperiodically within a small range. For the micro pores, there is no obvious regularity in the distribution of all three directions (Fig. 17 e-g). This is due to the random distribution of fibres in the fibre bundles and the insufficient resolution of micro pores.

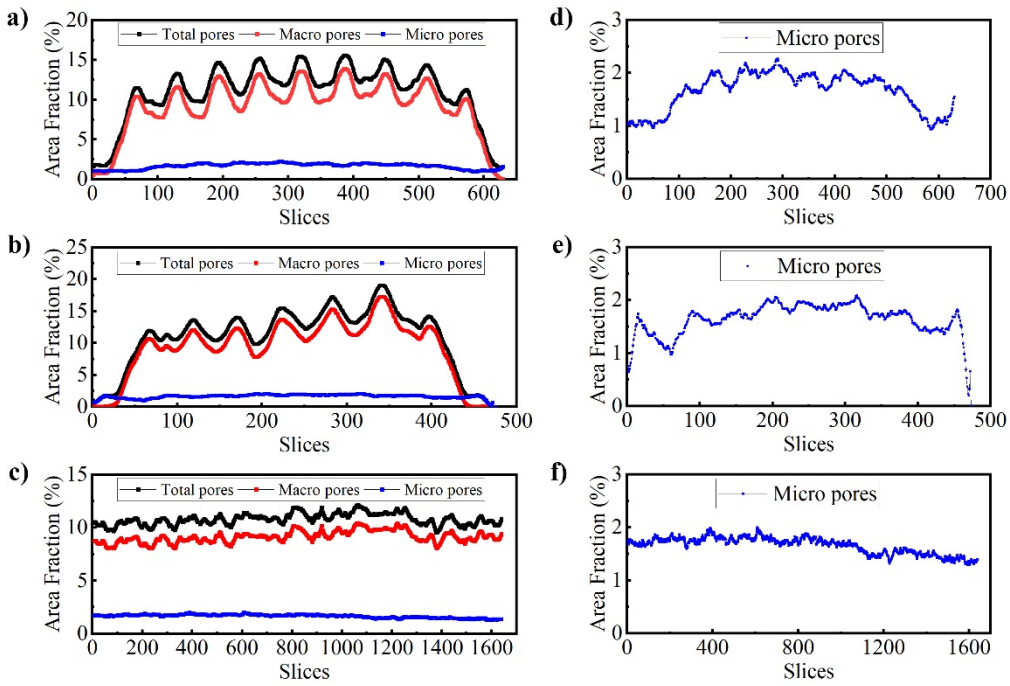

Fig. 3 Area fraction profiles as a function of the slice number in the three directions: a) XY slices; b) XZ slices c) YZ slices; d) micro pores in the XY slices; e) micro pores in the XZ slices; f) micro pores in the YZ slices